

Aerodynamic Stability of Bridge Stay Cables—Dynamic Tests and Simulations

PUBLICATION NO. FHWA-HRT-22-097

AUGUST 2022



U.S. Department of Transportation
Federal Highway Administration

Research, Development, and Technology
Turner-Fairbank Highway Research Center
6300 Georgetown Pike
McLean, VA 22101-2296

FOREWORD

Cable-stayed bridge configurations have become more common over the past several decades for bridges in the medium- to long-span range. The stay cables on these bridges are slender and flexible elements that are vulnerable to wind-induced vibration, potentially leading to safety, serviceability, and user comfort issues. Two of the significant types of wind-induced vibration are dry galloping and galloping in icing conditions. The Federal Highway Administration (FHWA) initiated this study to further investigate the effect of small deviations of the nominally circular cable cross section, a factor identified in recent research work as one of the important factors in galloping. This study is a significant step toward better prediction and prevention of aerodynamic issues on cable-stayed bridges. The results shed light on potential mitigation methods not only in design and retrofitting, but also in cable manufacturing, erection, and quality control. While additional research is recommended to develop appropriate models for analyzing and predicting vibration potential, the stability threshold demonstrated in this study may be an interim reference for reducing the risk of significant cable vibration before final design and analysis methods are available.

Cheryl Allen Richter, P.E., Ph.D.
Director, Office of Infrastructure
Research and Development

Notice

This document is disseminated under the sponsorship of the U.S. Department of Transportation in the interest of information exchange. The U.S. Government assumes no liability for the use of the information contained in this document. This report does not constitute a standard, specification, or regulation.

The U.S. Government does not endorse products or manufacturers. Trademarks or manufacturers' names appear in this report only because they are considered essential to the objective of the document.

Quality Assurance Statement

The Federal Highway Administration provides high-quality information to serve Government, industry, and the public in a manner that promotes public understanding. Standards and policies are used to ensure and maximize the quality, objectivity, utility, and integrity of its information. FHWA periodically reviews quality issues and adjusts its programs and processes to ensure continuous quality improvement.

Recommended citation: Federal Highway Administration, *Aerodynamic Stability of Bridge Stay Cables—Dynamic Tests and Simulations* (Washington, DC: 2022)
<https://doi.org/10.21949/1521926>.

TECHNICAL REPORT DOCUMENTATION PAGE

1. Report No. FHWA-HRT-22-097	2. Government Accession No.	3. Recipient's Catalog No.	
4. Title and Subtitle Aerodynamic Stability of Bridge Stay Cables—Dynamic Tests and Simulations		5. Report Date August 2022	
		6. Performing Organization Code	
7. Author(s) Guy L. Larose*, Stoyan Stoyanoff*, and Brian Dunn*		8. Performing Organization Report No.	
9. Performing Organization Name and Address Genex Systems 11848 Rock Landing Dr. Suite 303 Newport News, VA 23606 *Rowan Williams Davies & Irwin (RWDI) 600 Southgate Drive Guelph, ON, Canada N1G 4P6		10. Work Unit No. (TRAIS)	
		11. Contract or Grant No. DTFH61-13-D-00011	
12. Sponsoring Agency Name and Address Office of Infrastructure Research and Development Federal Highway Administration 6300 Georgetown Pike McLean, VA 22101-2296		13. Type of Report and Period Covered Laboratory Report 2017	
		14. Sponsoring Agency Code HRDI-40	
15. Supplementary Notes The Contracting Officer's Representative: Harold R. Bosch, HRDI-40.			
16. Abstract This project was a part of a multiyear, multipartner experimental investigation of the effects of wind on inclined stay cables that was initiated by the Federal Highway Administration (FHWA) in 2000. Between 2015 and 2017, the investigation on the galloping of inclined stay cables has focused on characterizing the influence of the cross-sectional shapes of stay cables, which have been observed to deviate from a perfect round shape, on the aerodynamics of the stays. This report documents the second phase of a project for this purpose. The first phase of the project, which started in 2015, included field measurements of cross-sectional shapes of stay cables and the measurements of their static aerodynamic force coefficients in a wind tunnel. The second phase covers dynamic tests on stay-cable replicas and the numerical simulation of their response to wind actions. Experimental results showed that for an inclination of 60 degrees at 0-degree yaw angle, large wind-induced oscillations were observed for most of the models and angles of attack investigated that could not be predicted solely based on the variations of the static force coefficients with Reynolds number and angles of attack. For these cases, increasing structural damping had only a small influence on the amplitude of the vibrations. For other orientations, inspection of the variations of the static coefficients with Reynolds number provided a good indication of the onset of the instability. For a cable model with helical fillets, increasing the Scruton number mitigated the vibrations. Comparison between experimental results and results from proposed numerical model showed that the three-dimensional, nonlinear, quasi-static modeling method can predict vibration vulnerability in some cases. Differences were observed in a cable-wind angle of 60 degrees and in cables with spatially variable cross-sectional shapes. Findings from numerical study included the following. Turbulence might be able to suppress the vibrations predicted in smooth flow. Numerically predicting aerodynamic vulnerability sometimes required a high resolution in parametric variation that would be difficult to achieve experimentally. One or more driving mechanisms for cable vibration might not have been identified, evidenced by an unexpected lack of influence from damping in some cases.			
17. Key Words Cable-stayed bridges, cables, vibrations, wind, rain		18. Distribution Statement No restrictions. This document is available to the public through the National Technical Information Service, Springfield, VA 22161. http://www.ntis.gov	
19. Security Classif. (of this report) Unclassified	20. Security Classif. (of this page) Unclassified	21. No. of Pages 64	22. Price

SI* (MODERN METRIC) CONVERSION FACTORS

APPROXIMATE CONVERSIONS TO SI UNITS

Symbol	When You Know	Multiply By	To Find	Symbol
LENGTH				
in	inches	25.4	millimeters	mm
ft	feet	0.305	meters	m
yd	yards	0.914	meters	m
mi	miles	1.61	kilometers	km
AREA				
in ²	square inches	645.2	square millimeters	mm ²
ft ²	square feet	0.093	square meters	m ²
yd ²	square yard	0.836	square meters	m ²
ac	acres	0.405	hectares	ha
mi ²	square miles	2.59	square kilometers	km ²
VOLUME				
fl oz	fluid ounces	29.57	milliliters	mL
gal	gallons	3.785	liters	L
ft ³	cubic feet	0.028	cubic meters	m ³
yd ³	cubic yards	0.765	cubic meters	m ³
NOTE: volumes greater than 1,000 L shall be shown in m ³				
MASS				
oz	ounces	28.35	grams	g
lb	pounds	0.454	kilograms	kg
T	short tons (2,000 lb)	0.907	megagrams (or "metric ton")	Mg (or "t")
TEMPERATURE (exact degrees)				
°F	Fahrenheit	5 (F-32)/9 or (F-32)/1.8	Celsius	°C
ILLUMINATION				
fc	foot-candles	10.76	lux	lx
fl	foot-Lamberts	3.426	candela/m ²	cd/m ²
FORCE and PRESSURE or STRESS				
lbf	poundforce	4.45	newtons	N
lbf/in ²	poundforce per square inch	6.89	kilopascals	kPa
APPROXIMATE CONVERSIONS FROM SI UNITS				
Symbol	When You Know	Multiply By	To Find	Symbol
LENGTH				
mm	millimeters	0.039	inches	in
m	meters	3.28	feet	ft
m	meters	1.09	yards	yd
km	kilometers	0.621	miles	mi
AREA				
mm ²	square millimeters	0.0016	square inches	in ²
m ²	square meters	10.764	square feet	ft ²
m ²	square meters	1.195	square yards	yd ²
ha	hectares	2.47	acres	ac
km ²	square kilometers	0.386	square miles	mi ²
VOLUME				
mL	milliliters	0.034	fluid ounces	fl oz
L	liters	0.264	gallons	gal
m ³	cubic meters	35.314	cubic feet	ft ³
m ³	cubic meters	1.307	cubic yards	yd ³
MASS				
g	grams	0.035	ounces	oz
kg	kilograms	2.202	pounds	lb
Mg (or "t")	megagrams (or "metric ton")	1.103	short tons (2,000 lb)	T
TEMPERATURE (exact degrees)				
°C	Celsius	1.8C+32	Fahrenheit	°F
ILLUMINATION				
lx	lux	0.0929	foot-candles	fc
cd/m ²	candela/m ²	0.2919	foot-Lamberts	fl
FORCE and PRESSURE or STRESS				
N	newtons	2.225	poundforce	lbf
kPa	kilopascals	0.145	poundforce per square inch	lbf/in ²

*SI is the symbol for International System of Units. Appropriate rounding should be made to comply with Section 4 of ASTM E380. (Revised March 2003)

TABLE OF CONTENTS

EXECUTIVE SUMMARY	1
Experimental campaign.....	1
Numerical simulations.....	2
CHAPTER 1. INTRODUCTION.....	3
Background	3
Objectives.....	5
CHAPTER 2. EXPERIMENTAL APPROACH.....	7
Scope of the Dynamic Tests.....	7
Description of the Experiments	7
Wind Tunnel Facility and Flow Conditions.....	7
Dynamic Rig	9
Model Fabrication, Geometry, and Properties	10
Test Program.....	14
CHAPTER 3. RESULTS OF THE EXPERIMENTS	17
Flat-face Reference Model	17
Cable Model IR113E-HF.....	19
Cable Model IR118E.....	22
Cable Model with Ice/wet-snow Accreted Shape	25
Conclusions of the experiments	30
CHAPTER 4. NUMERICAL SIMULATIONS	31
MOTIVATION	31
Methodology	31
Natural Wind Effects	31
Coordinate Framework	32
Linear Quasi-Static Formulation.....	34
Nonlinear Quasi-Static Formulation.....	35
Experiments.....	36
Results	37
Aerodynamic Damping.....	37
Discussions and conclusions	45
APPENDIX. TEST LOGS.....	47
REFERENCES.....	54

LIST OF FIGURES

Figure 1. Photo. View of the 2- by 3-m wind-tunnel test section with the false floor and ceiling installed.	8
Figure 2. Photo. View of the lower dynamic rig anchored to the wind-tunnel turntable.	9
Figure 3. Images. Sketches of the (a) ceiling and (b) floor dynamic rigs.	10
Figure 4. Image. Side-view sketch of the dynamic rig.	10
Figure 5. Image. Cross section of the Indian River Bridge, cable 118E, smooth surface.	11
Figure 6. Image. Cross section of the Indian River Bridge, cable 113E, helical fillets.	12
Figure 7. Illustration. Flat-face reference shape.	12
Figure 8. Illustration. Simplified ice/wet-snow accreted shape.	13
Figure 9. Photos. (a) View of cable model IR113E with helical fillets in the test section of the 2- by 3-m wind tunnel and (b) close-up view of the helical fillets.	15
Figure 10. Graph. Variations of the critical reduced velocity to exceed $0.5D$ amplitude as a function of Scruton number for the flat-face reference model at a cable-wind angle of 60 degrees.	17
Figure 11. Graph. Variations of the critical reduced velocity to exceed $0.7D$ amplitude as a function of Scruton number for the flat-face reference model in three segments at a cable-wind angle of 60 degrees.	19
Figure 12. Graphs. Variations of the (a) static lift coefficient, (b) static drag coefficient, and (c) dynamic response of cable model IR113E-HF as a function of Reynolds number for a cable-wind angle of 60 degrees and a Scruton number of 9.5.	20
Figure 13. Graph. Variations of the dynamic response of cable model IR113E-HF as a function of Reynolds number for a cable-wind angle of 60 degrees and three Scruton numbers.	21
Figure 14. Graph. Variations of the critical reduced velocity to exceed $0.5D$ amplitude as a function of Scruton number for the Indian River Bridge cable IR113E-HF model, with double helical fillets.	22
Figure 15. Graph. Variations of the critical reduced velocity to exceed $0.5D$ amplitude as a function of Scruton number for the Indian River Bridge cable IR118E model, smooth surface.	23
Figure 16. Graphs. Variations of the (a) static lift coefficient, (b) static drag coefficient, and (c) dynamic response of cable model IR118E as a function of Reynolds number for a cable-wind angle of 60 degrees and two Scruton numbers.	24
Figure 17. Graphs. Variations of the (a) static drag coefficient and (b) static lift coefficient for the cable model with simplified ice/wet-snow accreted shape as a function of Reynolds number and angles of attack for a cable-wind angle of 90 degrees.	25
Figure 18. Graphs. Variations of the (a) drag coefficient and (b) lift coefficient for the cable model with simplified ice/wet-snow accreted shape as a function of Reynolds numbers for selected angles of attack for a cable-wind angle of 90 degrees.	26
Figure 19. Illustration. Sketch of the simplified ice/wet-snow accreted shape marking the location of the angles of attack.	26
Figure 20. Graphs. Variations of the (a) static drag coefficient and (b) the static lift coefficient for the cable model with simplified ice/wet-snow accreted shape as a function of Reynolds numbers and angles of attack for a cable-wind angle of 60 degrees.	27

Figure 21. Graph. Variations of the critical reduced velocity to exceed $0.7D$ amplitude as a function of Scruton number for the cable model with simplified ice/wet-snow accreted shape.	28
Figure 22. Photo. View of the cable model with simplified ice/wet-snow accreted shape in the 2- by 3-m wind tunnel with a cable-wind angle equal to 90 degrees.	28
Figure 23. Photo. View of the cable model with simplified ice/wet-snow accreted shape in the 2- by 3-m wind tunnel with a cable-wind angle equal to 60 degrees.	29
Figure 24. Photos. (a) A side view and (b) a close-up view of the top end of the cable model with simplified ice/wet-snow accreted shape in the 2- by 3-m wind tunnel.	29
Figure 25. Illustration. Sketch of the three coordinate systems: global (or structural), wind, and cable (or body).	32
Figure 26. Illustration. Analyzed cross-section shapes: (a) IR113E-HF (exaggerated by a factor of 10) and (b) the flat-face symmetric cable.	37
Figure 27. Graphs. Across-wind aerodynamic damping predicted by equation 11 for (a) the total aerodynamic damping and (b) the contribution of each term.	38
Figure 28. Graph. Numerical simulations versus experimental results for Indian River Bridge cable IR113E-HF with $Sc = 5.3$ and yaw and inclination angles of 0 and 60 degrees, respectively.	39
Figure 29. Graphs. Comparison of numerical simulations to interpolated data for (a) drag and (b) lift coefficients for IR113E-HF for $\Phi = 60$ degrees and $Re = 2.4 \times 10^5$	40
Figure 30. Graphs. Time series of response for IR113E-HF at $\Phi = 60$ degrees and $Re = 2.4 \times 10^5$ with $Sc = 5.3$ where (a) is response plotted against time and (b) is y -response plotted against x -response with the same scale on both axes.	41
Figure 31. Graphs. The (a) aerodynamic damping (right axis) plotted with angle of attack α (left axis) for IR113E-HF at $\Phi = 60$ degrees and $Re = 2.4 \times 10^5$ with $Sc = 5.3$, combined with the relative probability (counts per bin/total) of the damping in (b) heave and (c) sway.	41
Figure 32. Graph. Comparison of numerical predictions to experimental results for the flat-face cable with $Sc = 17.5$ with initial angle of attack set to 20 degrees, and with yaw and inclination angles set to 0 and 60 degrees, respectively.	42
Figure 33. Graphs. Comparison of numerical simulations to experimental results for the flat-face cable of three rotated sections with initial angle of attack of (a) 80, 10, and 10 degrees and (b) 80, 30, and 80 degrees with $Sc = 20$ and yaw and inclination angles set to 0 and 60 degrees, respectively.	43
Figure 34. Graph. Comparison of numerical simulations to experimental results of IR113E-HF with $Sc = 5.2$ with initial angle of attack set to -55 degrees, and yaw and inclination angles set to 60 and 60 degrees, respectively.	44
Figure 35. Graph. Time series of response for IR113E-HF at $\Phi = 60$ degrees and $Re = 2.4 \times 10^5$ with $Sc = 5.3$ and $I_u \approx 5$ percent where (a) is response plotted against time and (b) is y -response plotted against x -response with the same scale on both axes.	45

LIST OF TABLES

Table 1. Summary of cable model properties.	13
Table 2. Combinations of angle of attack investigated.....	18
Table 3. Test log data for test number 1003.	48

LIST OF ABBREVIATIONS AND SYMBOLS

Abbreviations

3D	three dimensional
FHWA	Federal Highway Administration
HDPE	high-density polyethylene
HF	helical fillets
MDOF	Multi-degree of freedom

Symbols

C^*	generalized damping matrix
C_A, C_D, C_L	static force coefficients: A, along; D, drag; L, lift
D	cross-section depth or cable diameter
F^*	generalized forces
f	frequency
F_X, F_Y, F_Z	structural wind loads in cable loads coordinate system (body system)
I	identity matrix
I_u	intensity of turbulence in longitudinal wind direction
K^*	generalized stiffness matrix
m	cross-section mass per unit length
q, \dot{q}, \ddot{q}	generalized response: deflections, speeds, accelerations
R	radius
Re	Reynolds number (based on wind-tunnel reference speed)
Sc	Scruton number
T	coordinate transformation matrix
t	time
t_1, t_{max}	ice thickness
U_l, V_l, W_l	wind velocity vectors locally aligned with the cable loads
U_N	wind speed normal to cable
$U(t), W(t)$	time-varying components of wind
u, v, w	wind velocity vectors
u_s, v_s, w_s	wind velocity vectors locally aligned with structure
\bar{u}	mean wind speed in longitudinal wind direction (reference speed in wind tunnel)
V/fD	critical reduced velocity
V	mean wind speed in longitudinal wind direction at which the cable reached an aerodynamic stability boundary
X, Y, Z	cable loads coordinates in body system
x, y, z	structural coordinates/response deflections
$\dot{x}, \dot{y}, \dot{z}$	speed of structural response
x', y', z'	wind coordinates
$\alpha(t)$	instantaneous variation of angle of local wind attack
α	angle of local wind attack: section rotation about its longitudinal axis
β	wind direction angle (yaw)
β_0	mean wind direction
ζ	structural damping (ratio to critical)

ζ_{aero}	aerodynamic damping (ratio of critical)
θ	cable inclination angle from the horizontal plane
θ_0	mean cable inclination angle
μ	air dynamic viscosity
ν	air kinematic viscosity
ρ	air density
σ_u	standard deviation (root-mean-square) of turbulence in longitudinal wind direction
Φ, ϕ	effective cable-wind angle
ω_n	circular frequency of the n th cable mode

EXECUTIVE SUMMARY

The Federal Highway Administration (FHWA) conducted an experimental and numerical study of the inclined cable-galloping phenomenon applied to the design of stay cables for cable-stayed bridges. This report presents a detailed description of the experimental and numerical approaches, the main findings of the study, and future recommendations. The study was carried out in two parts.

EXPERIMENTAL CAMPAIGN

Experiments on free-to-respond rigid bridge stay cable models were carried out in a 2- by 3-m wind tunnel. The models were set at an inclination of 60 degrees and were yawed to the flow from 0 to 90 degrees to study the influence of the cable-wind angle on the wind-induced excitation. The models were designed so that they could be rotated along their longitudinal axis to set their angle of attack as desired. The experiments were set as a logical progression of a concerted research effort that included:

- The full-scale measurements of the cross-sectional shape of high-density polyethylene (HDPE) external sheathing of stay cables for bridges in service in the United States by FHWA.⁽¹⁾
- Static tests on replicas of the scanned shapes to characterize the variations of the cross-sectional aerodynamic coefficients of the stay cables as a function of Reynolds number, angle of attack, and cable-wind angle. The tests were carried out in 2015 in the 2- by 3-m wind tunnel and are detailed in a 2021 report from FHWA.⁽²⁾
- The current dynamic tests on the same models.

The final phase of experiments focused on the verification, through dynamic tests on the stay-cable replicas, of the range of applicability of the quasi-steady theory for the predictions of the damping level needed to control the vibrations of stay cables with shape distortion and/or with ice/wet-snow accretion. The 1.8-m-long models were supported in a 16-spring dynamic rig, which utilized air bearings and eddy-current dampers. The mass-damping parameter (Scruton number), the Reynolds number, the reduced velocity, and the surface-roughness-to-diameter ratio of the models were adjusted to match full-scale values.

Five cable models were investigated, including a section with a generic ice/wet-snow accretion. Galloping was observed for all models for a variety of cable-wind angles, Scruton numbers, and angles of attack. In general, based on the variations of the static force coefficients with angles of attack and Reynolds numbers, the onset speed of the instability could be predicted. However, for a cable-wind angle of 60 degrees, large wind-induced oscillations were observed in several instances that could not be predicted solely based on the variations of the static force coefficients with Reynolds number and angles of attack. For these cases, increasing structural damping (the typical measure used for vibration control) had only a limited influence on the amplitude of the vibrations. This phenomenon was not observed for the cable-wind angles greater than 60 degrees that were investigated.

For the cable model with helical fillets (HF), increasing the Scruton number was observed to mitigate the vibrations as was first anticipated at the onset of the study.

NUMERICAL SIMULATIONS

To expand the use of the experimental data, a theoretical framework via numerical simulations of cable response was investigated. Predictions of the dynamic response of the cable models used in the experiments were carried out using a three-dimensional (3D), nonlinear response analysis simulation in the time domain. The simulations modeled with precision the dynamics of the mechanical systems, including mass, stiffness, frequencies, and structural damping.

The aerodynamics were modeled through the static force coefficients and their rate of change with varying angles of attack, Reynolds numbers, and cable-wind angles. The coefficients were measured on the same models in the same wind tunnel in a test campaign conducted in 2015.⁽²⁾ By direct comparison with the dynamic tests, the simulations provided an evaluation of the range of applicability of the quasi-steady theory for the predictions of negative aerodynamic damping for stay cables with shape distortions due to sheathing deviations and/or ice/wet-snow accretions.

Using a 3D nonlinear quasi-static approach, the predictions were generally in good agreement with the wind-tunnel experiment observations. Numerical tests showed that turbulence might be able to suppress the vibrations predicted in smooth flow. In other cases, especially for a cable-wind angle of 60 degrees, the comparisons showed that the proposed aerodynamic model cannot explain the wind-tunnel results. The likely reasons for these discrepancies are:

- Lack of details in the static force coefficients data. Very sharp gradient trends were seen in the transitions from stable to unstable regions and vice versa that required detailed knowledge of the force coefficients over the three-parameter space: angle of attack, cable-wind angle, and Reynolds number. Even though very fine increments of angle of attack (e.g., approximately 1 degree) have been measured in some cases, it is practically challenging to sample the entire parameter space experimentally.
- Different aerodynamic phenomena caused the instabilities. Some of the large-amplitude vibrations found during the test could not be predicted and/or did not follow the general expectations based on quasi-static theory. For example, physical tests with increased damping in the wind tunnel have shown a limited influence of the added damping on the oscillations, even at high levels of Scruton number. These observations indicate that another aerodynamic excitation mechanism (perhaps stiffness driven) may play a significant role in the observed responses. Identifying and modeling aerodynamic phenomena outside of those phenomena described by quasi-static theory was beyond the scope of the current research program.

CHAPTER 1. INTRODUCTION

The Federal Highway Administration (FHWA) conducted an experimental and numerical study of the inclined cable-galloping phenomenon applied to the design of stay cables for cable-stayed bridges. This study is a continuation of a multiyear multipartner experimental investigation of the effects of wind on inclined stay cables that FHWA initiated in 2000.

The study reported here is a logical progression of the concerted research effort between 2015 to 2017 that included:

- The full-scale measurements of the cross-sectional shape of high-density polyethylene (HDPE) external sheathing of stay cables for bridges in service in the United States by FHWA.⁽¹⁾
- Static tests on replicas of the electronically scanned shapes to characterize the variations of the cross-sectional aerodynamic coefficients of the stay cables as a function of Reynolds number, angle of attack, and cable-wind angle.⁽²⁾
- The current dynamic tests on the same models in the same wind tunnel and numerical simulations of the observed wind-induced response.

This report presents the results of the dynamic tests, including a detailed description of the experimental and numerical approaches, the main findings of the study, and recommendations for a way forward to evaluate the damping demands to mitigate inclined stay-cable galloping for cable-stayed bridges.

BACKGROUND

In recent years, it has been observed that the external sheathings used to cover the steel strands of stay cables of cable-stayed bridges were not necessarily of regular circular shape, as many researchers had assumed. Today, and for the past 15–20 years, the preferred material used for the sheathing has been HDPE, the same material and pultrusion process used for pipes to carry water or natural gas in industrial applications.

The external shape of the sheathing is generally controlled, with deviation tolerances ranging from ± 1.5 to ± 5 percent of the mean diameter, depending on the application and the quality standard followed. Onsite, however, depending on the shipping and storage conditions of the HDPE tubes (generally 12-m long), deviations larger than ± 5 percent of the mean diameter can exist, and typically, if the deviations are larger than ± 10 percent of the mean diameter, the tube is discarded since welding to another tube might not be possible.

In a broad sense, imperfections of the cross sections of the stays of approximately 1–2 percent of the mean diameter (i.e., 2 to 4 mm for a 200-mm HDPE tube) should not be a concern on a cable-stayed bridge with a 350-m main span and 150-m tower heights. However, the combination of the diameter of the stays and the typical wind speeds of the atmospheric boundary layer put the stays right in the critical Reynolds number regime. In this regime, many fluid mechanics phenomena happen at the surface of a circular cylinder affecting the behavior of

the boundary layers, the shear layers, the pressure distribution, and the wind loading. These phenomena are known to be influenced by Reynolds number, surface irregularities and imperfections, the characteristics of the turbulence of the flow, the angle of incidence between the flow and the circular cylinders, and other factors. Schewe states that in the critical Reynolds number regime, “a very small cause can have a very great effect.”⁽³⁾ For a thorough review of the problem specifically related to inclined stay cables, the reader is referred to the work of Christiansen, and for circular cylinders in general to Zdravkovich.^(4,5)

In 2015, FHWA initiated a research study in three parts, following up on a series of laboratory experiments on a mock-up of a stay cable in a dynamic suspension rig that clearly identified that the eccentricity of a cable could lead to instability.⁽⁶⁾ The first part consisted of the development of a scanning robot that could climb up existing stay cables and provide details of the cross-sectional geometry and surface conditions. The robot was then put into service, and multiple cables of several bridges were scanned in the United States over a 2-yr period. Preliminary results of these scans were published by FHWA in a conference paper.⁽¹⁾ In general, the stay cables were found to have a cross-sectional shape that deviated from a round circular cylinder. The out-of-roundness level varied significantly from cable to cable and from section to section on the same cable.

The second part of the FHWA research project consisted of a series of wind-tunnel tests on replicas, at model scale, of the shapes of the external sheathing of cables provided by FHWA from direct measurements on existing bridges. The tests were carried out in a 2- by 3-m wind tunnel in the summer of 2015. The models were kept stationary, and the aerodynamic forces as a function of Reynolds number, angles of attack, and cable-wind angle were monitored with two internal force balances, one at each extremity of the models. These tests are referred to as the “static tests.”

Among other observations, the tests confirmed that the aerodynamic characteristics of the stays were highly sensitive to their cross-sectional shape variation.^(2,4) A small deviation from the mean curvature had an important influence on the aerodynamic force coefficients, especially for the mean across-wind force coefficients in the critical Reynolds number regime. Based on an analysis of the force coefficients, negative aerodynamic damping in excess of 1 percent of critical was derived analytically from the static tests, indicating the potential of stay cables to gallop at certain cable-wind angles, Reynolds numbers, and cross-sectional irregularities.⁽⁴⁾

The third part of the FHWA research project was to verify through dynamic tests that the sensitivity to wind-induced vibrations and inclined cable galloping predicted based on the static tests would be confirmed on free-to-respond models with the same cross-sectional shapes. This final part forms the basis for the experimental part of the study reported here.

Moreover, the estimated damping demands based on the static tests carried out in 2015 indicated the possibility of cable dampers on bridges built according to the current designed practice not being fully capable of mitigating wind excitations.⁽²⁾ Thus far, however, there is no strong evidence of unexplained and/or difficult-to-control vibrations with dampers on the existing bridges. Questions do arise, however. What are these unaccounted for conditions which work in favor of mitigating the destabilizing effects of the cable sheathing imperfections? Is there a

missing component in our design methodology that needs improvement? These questions are also covered in the current study.

OBJECTIVES

The experiments' main objective was to study how replicas of existing stay cables would respond to the potential for aerodynamic instabilities as revealed by their static force coefficients when suspended in a 2-degree-of-freedom suspension system with adjustable frequencies and structural damping. The main objective of the numerical simulations of the experiments was to provide an evaluation of the range of applicability of the quasi-steady theory for the predictions of negative aerodynamic damping for stay cables with shape distortions due to sheathing deviations and/or ice/wet-snow accretions.

CHAPTER 2. EXPERIMENTAL APPROACH

SCOPE OF THE DYNAMIC TESTS

To ensure that the experimental conditions of the dynamic tests would be identical to the conditions at which the static tests were carried out, the experiments were designed to take place in the same wind tunnel, on the same models, in the same flow conditions and at the same Reynolds numbers as in the 2015 study.⁽²⁾

A total of four cross-sectional shapes were studied on five different models. The main part of the experiments was carried out on:

- The cross-sectional shapes from a lower section of cables numbered 118E and 113E of the Indian River Inlet Bridge (officially known as the Charles W. Cullen Bridge), located 7 miles south of the city of Rehoboth Beach, DE in Delaware Seashore State Park. For this study, cable 118E was modeled as a smooth surface and cable 113E was modeled as having double helical fillets (HF). All cables of the Indian River Inlet Bridge have double helical fillets.
- A reference shape developed in the framework of the static tests identified as a “flat-face” cross section.^(2,4)
- A simplified generic ice/wet-snow accreted shape developed in the framework of the current study.

All models had a constant cross-sectional shape for their entire length, except for one model that was built in three sections. For the model in three sections, each section had the flat-face shape that could be rotated around its longitudinal axis to adjust its angle of attack independently of the two other sections. The idea behind this model with three sections was to study the influence of changes of cross section on the aerodynamic instabilities, thus making a parallel with the fabrication and installation methods of stay cables that are generally enclosed in several HDPE tubes 11- to 12-m long. The field measurements and other site observations have revealed that each 12-m section may have a different cross-sectional shape and/or be rotated along its longitudinal axis thus having different aerodynamic properties for a given oncoming wind alignment.

The experiments were designed to respect the following similitude requirements: Reynolds number, mass-damping parameter, and reduced velocity.

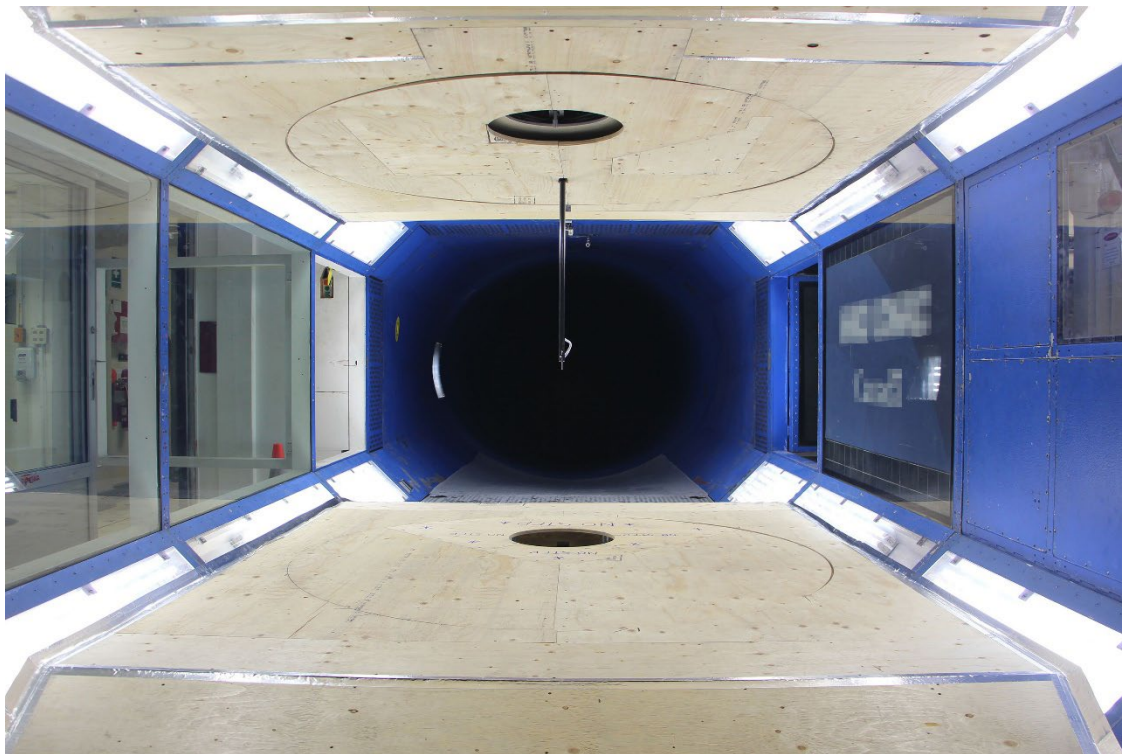
DESCRIPTION OF THE EXPERIMENTS

Wind-Tunnel Facility and Flow Conditions

The measurement campaign took place in a 2- by 3-m wind tunnel. The wind tunnel is a closed-circuit atmospheric facility with an empty test section that measures 2.7-m wide by 1.9-m high by 5.2-m long and has a 9:1 contraction ratio. The wind tunnel has a wind speed uniformity of ± 0.7 percent and a turbulence level of 0.14 percent in an empty test section. The wind tunnel

is equipped with floor and roof turntables allowing precise yawing of models mounted vertically in the test section. The maximum speed of the wind tunnel (120 m/s) and the size of the test section are suitable for testing model-scale stay cables with a high aspect ratio at full-scale Reynolds numbers. For an elastically supported rigid sectional model, Froude number scaling did not play a role and was not considered. In the field, gravity will influence the sag of the cables, affecting their frequency in one plane. This effect is simulated in the wind tunnel by a different frequency between heave and sway motion. The similitude parameters that were respected in the experiments were reduced velocity (which governed the velocity and frequency scaling), mass-damping parameter (Scruton number, Sc), and Reynolds number (Re).

The wind speeds considered in the experiment ranged from 10 to 80 m/s. This range allows testing in the Reynolds number regime of interest. A false floor and false ceiling were installed in the wind tunnel to shield the test rig from the flow, as shown in figure 1. The false floor and ceiling consisted of a 15-degree ramp upstream of the model, a flat section measuring 2.9-m long, and a 15-degree ramp downstream of the model. The height of the wind tunnel was reduced to 1.53 m with the false ceiling and floor installed. The rotating portion of the false floor and ceiling allowed the model to be yawed from 0 to 90 degrees. The false floor and ceiling each included a 0.45-m-diameter hole. The hole was necessary to allow the cable to move, unimpeded, with amplitudes of up to ± 1.7 cable diameters.



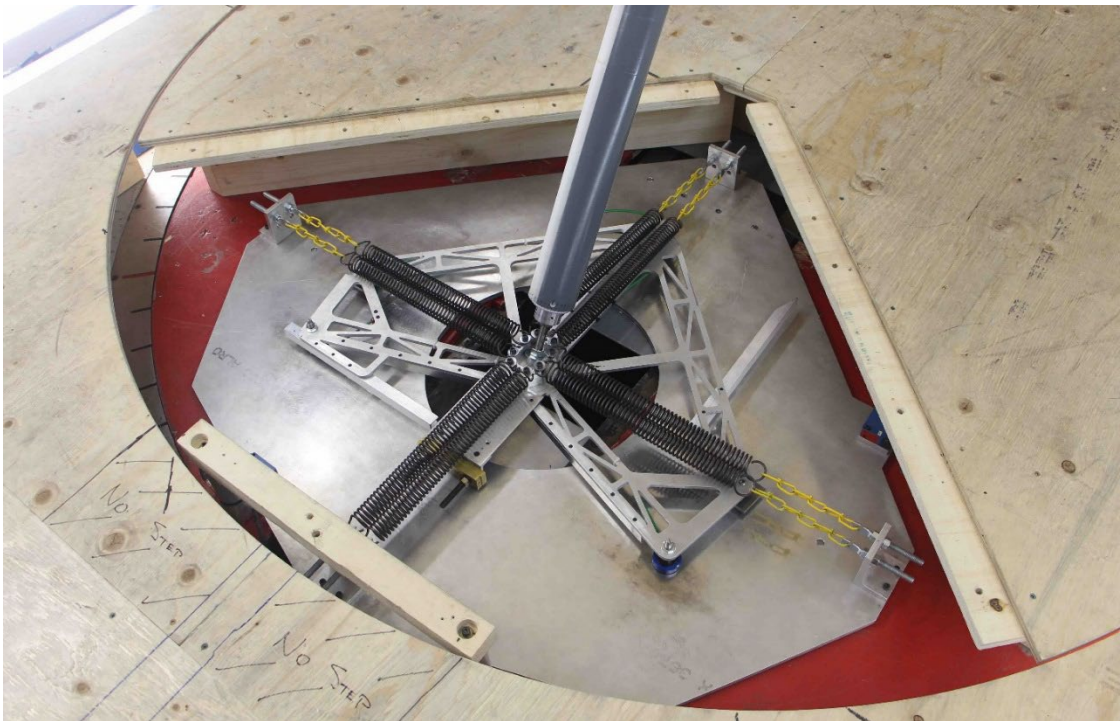
© 2017 RWDI.

Figure 1. Photo. View of the 2- by 3-m wind-tunnel test section with the false floor and ceiling installed.

Dynamic Rig

A 16-spring suspension rig was developed and built to fit within the false floor and ceiling of the 2- by 3-m wind tunnel. Six air bearings were used to suspend the models within the arrays of springs so that the models could move freely in the along-wind (heave mode of an inclined stay cable) and the across-wind (sway mode) directions. The rig was designed to allow vibration amplitudes of up to 1.7 cable diameters (150 mm). A combination of spring stiffness and tension was used to adjust the frequency of oscillation in each of the modes.

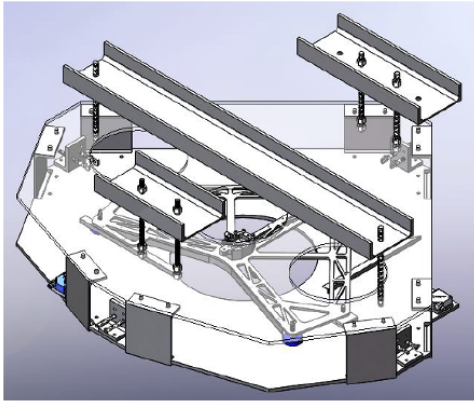
The rig was designed to include four eddy-current dampers that provided a damping level constant with amplitude of motion and could be adjusted independently for each mode of vibration. Figure 2 presents a view of the lower rig anchored to the turntable of the wind tunnel, with a panel of the false floor removed. Four laser displacement transducers monitored the motion of the cable models at their extremities. For some of the experiments, two of the springs in each degree of freedom were replaced by load cells, converting the dynamic rig into a static rig to determine the static force coefficients of the cable model with the same end conditions as for the dynamic tests. Sketches of the dynamic rig are shown in figure 3 and figure 4.



© 2017 RWDL.

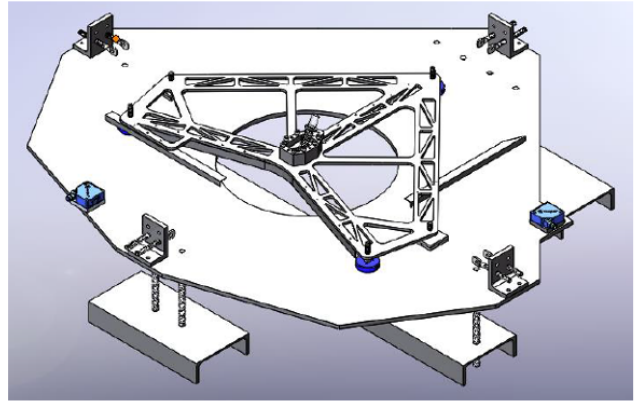
Figure 2. Photo. View of the lower dynamic rig anchored to the wind-tunnel turntable.

CEILING RIG:



(a)

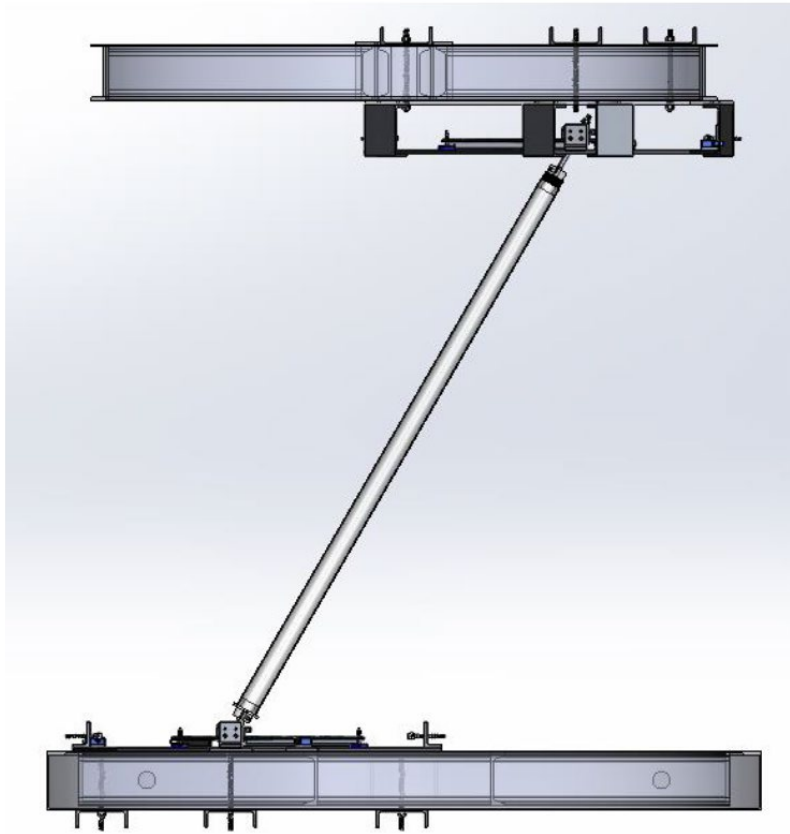
FLOOR RIG:



(b)

Source: FHWA.

Figure 3. Images. Sketches of the (a) ceiling and (b) floor dynamic rigs.



Source: FHWA.

Figure 4. Image. Side-view sketch of the dynamic rig.

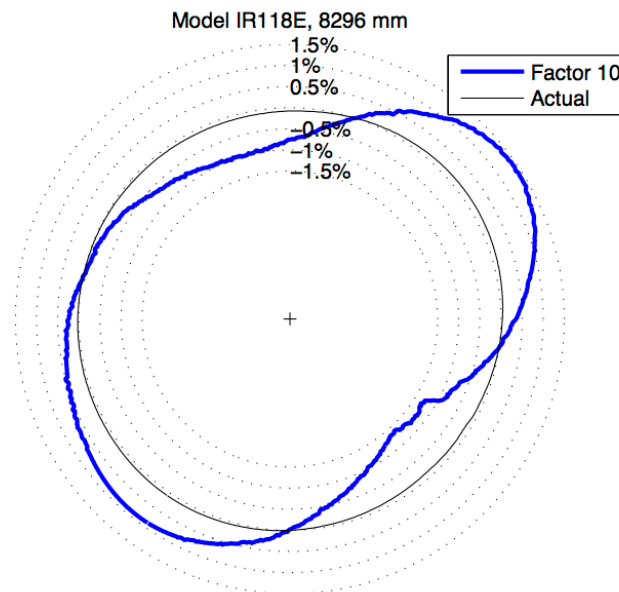
Model Fabrication, Geometry, and Properties

The models were designed and fabricated using the same technique developed for the static tests detailed in the 2021 report.⁽²⁾ Selective Laser Sintering was used to grow cable model tubes that

were inserted onto a stiff carbon fiber spar. The tubes for the Indian River Bridge representative cables and the flat-face reference shape of the static tests were extended to 1.8 m to match the longer models of the dynamic tests, as opposed to 1.5 m for the static tests. These models had a diameter (D) of 0.089 m and an aspect ratio of 20. Two new models with a smaller diameter were built for the ice/wet-snow accreted shape ($D = 0.070$ m) and the flat-face shape ($D = 0.070$ m) in three sections. The research team anticipated that the drag crisis would occur at lower Reynolds numbers for the ice/wet-snow accreted shape; therefore, the decision was made to reduce the diameter of the model.

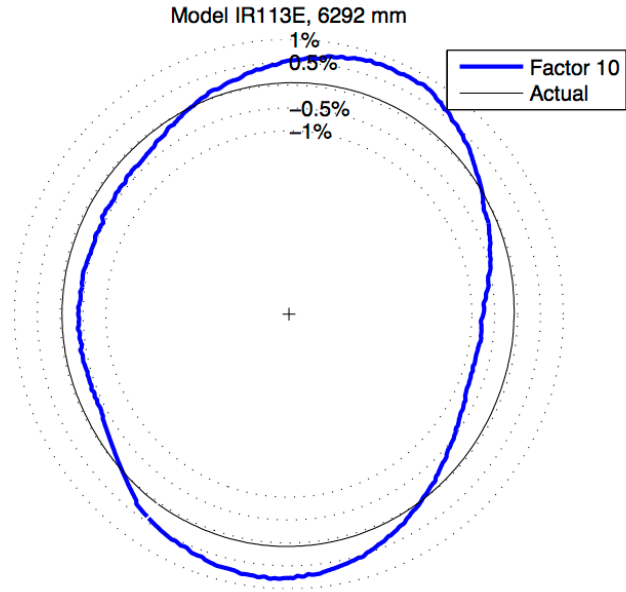
The surface-roughness-to-diameter ratio of the models was adjusted to an average of 1.5×10^{-5} , similar to the surface roughness of prototype cables. A rotation of the cable tube on the longitudinal axis of the spar was used to adjust the angle of attack of the model. A simultaneous rotation of the floor and roof turntable was used to set the yaw angle. The inclination of the model was kept constant at 60 degrees.

Figure 5 through figure 8 present the cross-sectional shapes of the cable models of the dynamic tests. A summary of the model properties, including mass per unit length (m) and frequency (f) in both the sway and heave directions, is presented in table 1.



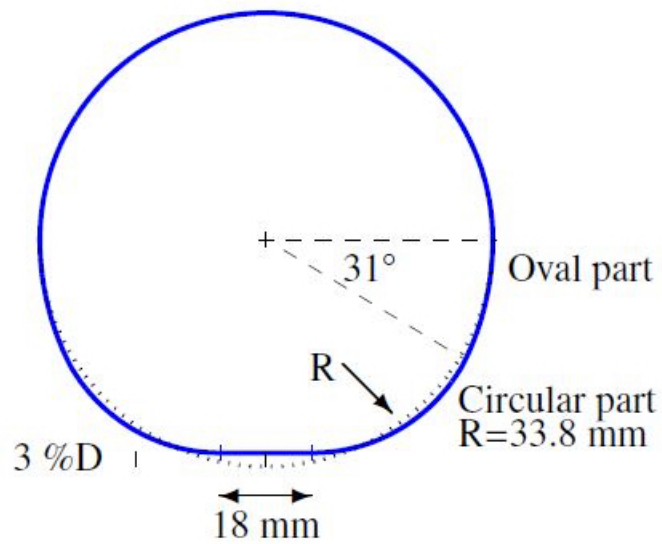
Source: FHWA.

Figure 5. Image. Cross section of the Indian River Bridge, cable 118E, smooth surface.



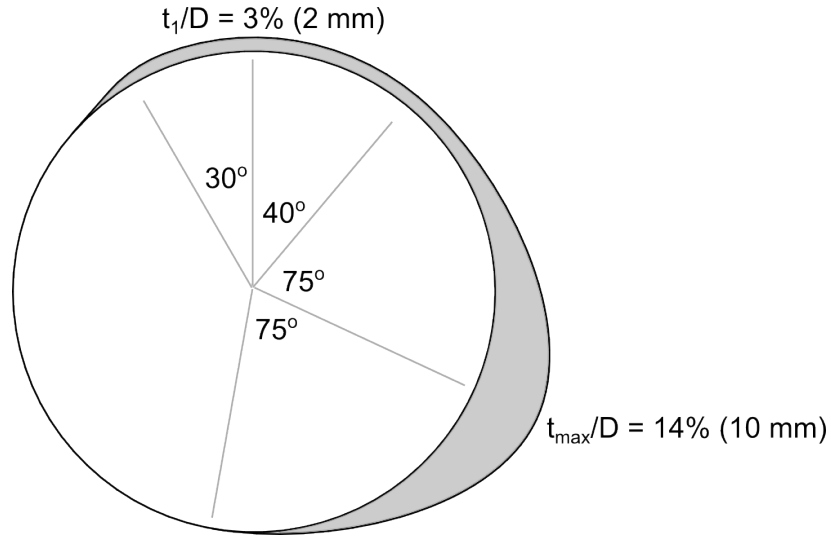
Source: FHWA.

Figure 6. Image. Cross section of the Indian River Bridge, cable 113E, helical fillets.



Source: FHWA.

Figure 7. Illustration. Flat-face reference shape.



Source: FHWA.

Note: t_1 represents average ice thickness, t_{max} represents maximum ice thickness.

Figure 8. Illustration. Simplified ice/wet-snow accreted shape.

Table 1. Summary of cable model properties.

Properties	IR118E	IR113E HF	Flat-Face	Flat-Face 2	Ice/Wet-snow
D (m)	0.089	0.089	0.089	0.065	0.070
m_{sway} (kg/m)	7.63	7.67	7.62	5.71	5.94
m_{heave} (kg/m)	7.42	7.46	7.41	5.50	5.73
f_{sway} (Hz)	4.40	4.35	4.41	5.00	4.92
f_{heave} (Hz)	4.23	4.17	4.13	4.76	4.70
Damping (percent of critical)	1.1–5.9	0.6–2.5	0.3–2.1	1.6–3.3	0.4–1.5
Sc range	8.4–46.4	4.7–19.7	2.0–16.5	14.7–31.4	3.9–15.2
Re range ($\times 10^5$)	0.3–3.6	0.6–4.1	0.3–3.4	0.7–3.3	0.4–4.1

A structure's aerodynamic stability is governed by the characteristics of its main components and will depend on each of the following: cross-sectional geometry, mass, and structural properties such as stiffness and damping. For any element of the structure, the dependence on overall dimensions, mass and damping can be described by the mass-damping parameter known as the Scruton number, Sc :

$$Sc = \frac{m\zeta}{\rho D^2} \quad (1)$$

Where:

m = mass per unit length.

ζ = structural damping (ratio to critical).

ρ = air density.

D = section depth or cable diameter.

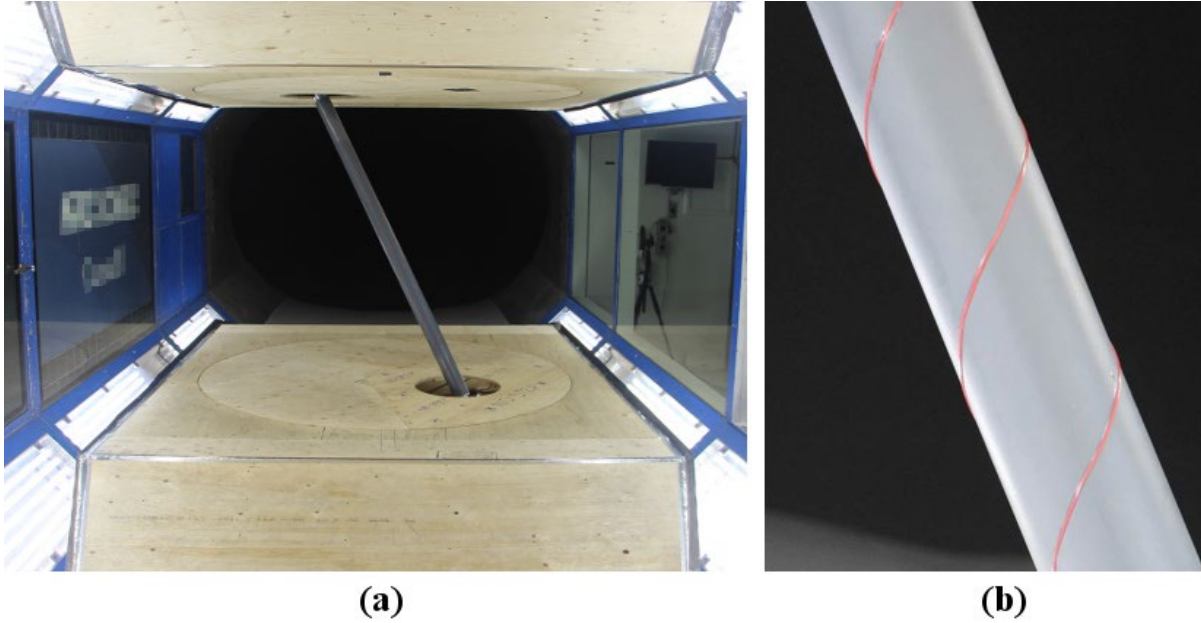
In general, a lower Scruton number implies that a structural component might be more susceptible to aerodynamic instabilities due to its low mass per unit length and/or damping relative to the overall dimensions exposed to wind.

In this study, the models were kept light in relation to their diameter compared to expected full-scale values. To respect mass-damping similarity, the mass-damping parameter was adjusted by compensating with added structural damping.

The generic ice/wet-snow accreted shape was developed based on field observations and experience. It represents the shape of a stay cable following a freezing rain event where a 2-mm layer of glaze ice would have accreted on a large part of the circumference (220 degrees), followed by a small drop of temperature where the freezing rain would have transformed into wet-snow and 8 mm of wet-snow would have accumulated on the windward face of the cable. Accretions of glaze ice and wet-snow on cables are common for cables in moderate and continental climates.

Test Program

During the static tests in 2015, critical cable-wind angles and angles of attack were identified as having a potential for aerodynamic instability. The dynamic tests systematically revisited these critical conditions for the two Indian River Bridge cable models and the flat-face reference shape. When vibrations were observed, the level of structural damping and Scruton number were increased to evaluate the influence of damping on the vibrations and to compare them with predictions of damping demand based on a quasi-steady aerodynamic model.⁽⁷⁾ The tests consisted of speed sweeps at fixed angles of attack, yaw angles, and damping levels. A view of the test arrangement is shown in figure 9. The list of runs for each model is presented in table 3 of Appendix A along with a summary of the test conditions.



© 2017 RWDI.

Figure 9. Photos. (a) View of cable model IR113E with helical fillets in the test section of the 2- by 3-m wind tunnel and (b) close-up view of the helical fillets.

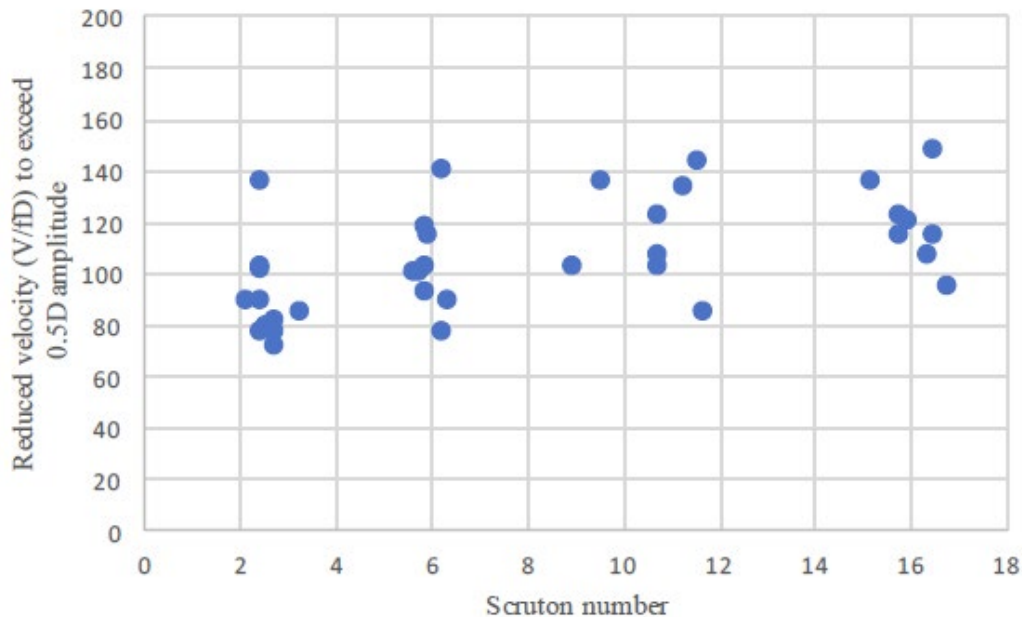
A similar approach was taken for the flat-face model in three sections. The angle of attack of each section was deliberately selected to alternate between an angle deemed potentially unstable and an angle deemed stable. This approach was followed by tests with a random selection of the angles of attack for each section. For the ice/wet-snow accreted shape, the dynamic rig was converted to a static rig to determine the static force coefficients as a function of angle of attack before dynamic tests were conducted with this model. Inspection of the static coefficients was subsequently used to choose the critical angles for dynamic tests. Dynamic tests for the ice/wet-snow accreted shape were repeated for various level of damping.

CHAPTER 3. RESULTS OF THE EXPERIMENTS

The main findings of the experiments presented in this chapter focus on the influence of the Scruton number on the wind-induced vibrations observed. The experimental data, digital photos, and videos for each run described in the appendix were stored on an external hard drive and provided to FHWA under separate cover.

FLAT-FACE REFERENCE MODEL

Figure 10 presents the variations of the critical reduced velocity (V/fD) at which the vibrations observed exceeded 50 percent of the model diameter (written as $0.5D$ in the figure captions) with Scruton number and angle of attack for the flat-face reference model. The turntable was kept at 0 degrees for the experiments, and the model inclination was 60 degrees, resulting in a cable-wind angle of 60 degrees. Ten angles of attack were investigated. Instability in the across-wind direction (sway mode) was observed for all angles of attack investigated for Scruton numbers varying from 2.2 to 16.5. In general, the amplitude of the vibrations grew gradually with increasing wind speed until amplitudes of 1 cable diameter were reached.



Source: FHWA.

Figure 10. Graph. Variations of the critical reduced velocity to exceed $0.5D$ amplitude as a function of Scruton number for the flat-face reference model at a cable-wind angle of 60 degrees.

In figure 10, the variations observed in critical reduced velocity for a fixed Scruton number revealed that the cross-sectional shape had an important influence on the amplitude of the vibrations observed. However, the relatively low increase of the critical reduced velocity with Scruton number for all angles of attack, indicated that damping had a weak influence on the

instability process which is not in agreement with predictions that would be based on a quasi-steady aerodynamics process. This finding agrees with the work of Kimura, Kato, and Kubo.⁽⁸⁾

A similar trend was observed for the flat-face reference model in three segments. Apart from 2 randomly selected combinations of angles of attack, all combinations tested (13) were unstable and remained unstable up to a Scruton number above 35. The combinations of angle of attack investigated are shown in table 2.

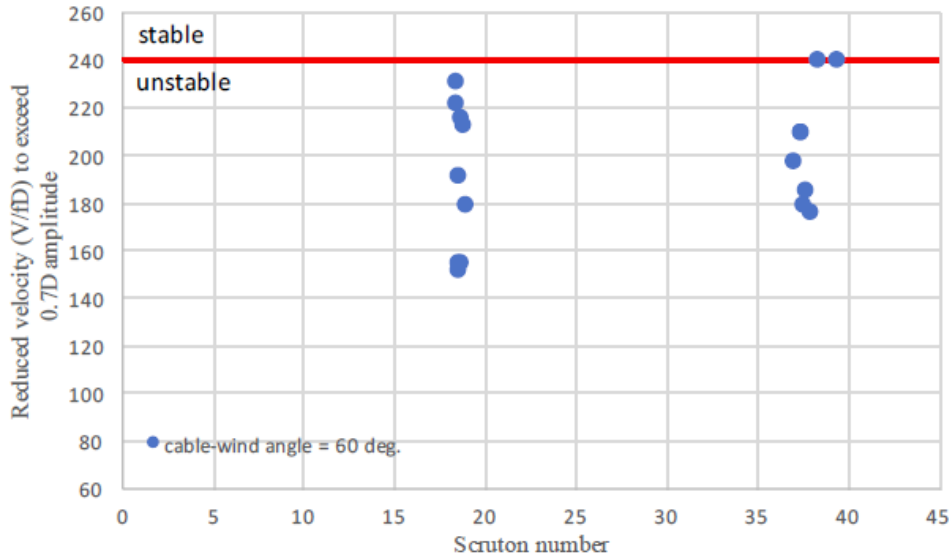
Table 2. Combinations of angle of attack investigated.

Run	Bottom Section (Degree)	Midsection (Degree)	Top Section (Degree)
409	20	20	20
412	80	80	80
417	120	120	120
423	20	80	120
426	20	120	80
429	120	80	20
434	120	20	80
446	10	100	40
448	60	80	30
451	80	10	10
455	80	30	80
458	100	40	100
461	120	20	0

For example, for run 409, all three sections of the model were set at an angle of attack of 20 degrees. For run 423, the lower section of the model was set at an angle of attack of 20 degrees, the midsection at 80 degrees and the top section at 120 degrees.

The results are summarized in figure 11. However, the tests revealed that the critical reduced velocity at which the vibrations would be unstable was greatly influenced by the combination of angles of attack of the three segments. As shown in figure 11, for a Scruton number of 17, the critical reduced velocity increased from 150 up to 230 (240 was defined as the stability threshold) by a rotation of the angles of attack. The selected stability threshold corresponds to the maximum wind speed reached in the experiments where the cable model was still stable. It is assumed that the cable would still be stable beyond this wind speed.

Note that the increase of reduced velocity in the wind tunnel was achieved by gradually increasing the mean wind speed of the flow. Aerodynamic stability was observed for two combinations of angles where two of the segments were set at the same angle of attack. This observation clearly indicated that the spanwise correlation of the aerodynamic forces had an importance on the instability observed.



Source: FHWA.

Figure 11. Graph. Variations of the critical reduced velocity to exceed 0.7D amplitude as a function of Scruton number for the flat-face reference model in three segments at a cable-wind angle of 60 degrees.

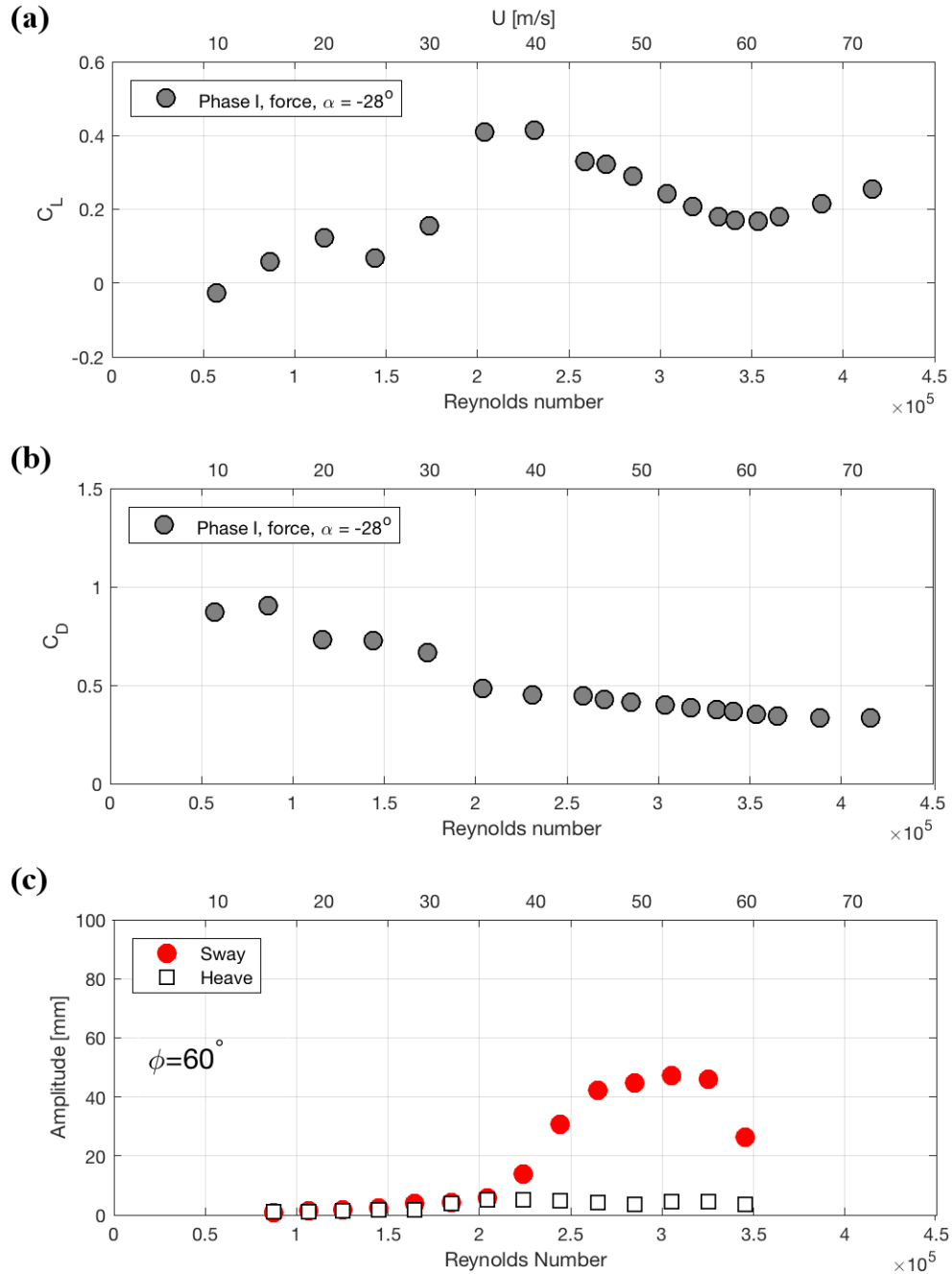
CABLE MODEL IR113E-HF

The results for the Indian River Bridge cable IR113E-HF are presented in figure 12 through figure 14. Instabilities were observed in sway for most of the angles of attack tested for a cable-wind angle of 60 degrees and a Scruton number of 5. The instabilities followed the pattern that the test team had anticipated based on the variations of the force coefficients with Reynolds number.

Typically, oscillations started after a drop of the drag coefficient and a sudden increase of the lift coefficient. The oscillations reached their maximum with an increase of Reynolds number, a reduction of the drag coefficient, and a reduction of the lift coefficient. The oscillations finally subsided when the Reynolds number reached a region where the lift coefficient was at a minimum and the drag coefficient reached a plateau or re-increased. When oscillations occurred, they appeared to be in sync with the formation of a laminar separation bubble on one side of the cable (also known as the start of the TrBL1 regime based on Zdravkovich's nomenclature) and continued until the disruption of the laminar separation bubble.⁽⁵⁾

For a smooth cable in the critical regime, oscillations that would start and stop in regions of transition between TrBL0 and TrBL1 or TrBL1 and TrBL2, have been reported on several occasions. Such oscillations have been well documented in previous studies initiated by FHWA.⁽⁶⁾ The observations of the current study confirmed that this transition process (and therefore source of dynamic excitation) was also present for a cable shape directly obtained from a stay cable in service and with typical helical fillet of approximately 1.5- to 2.5-mm thickness at a 45-degree helix angle.

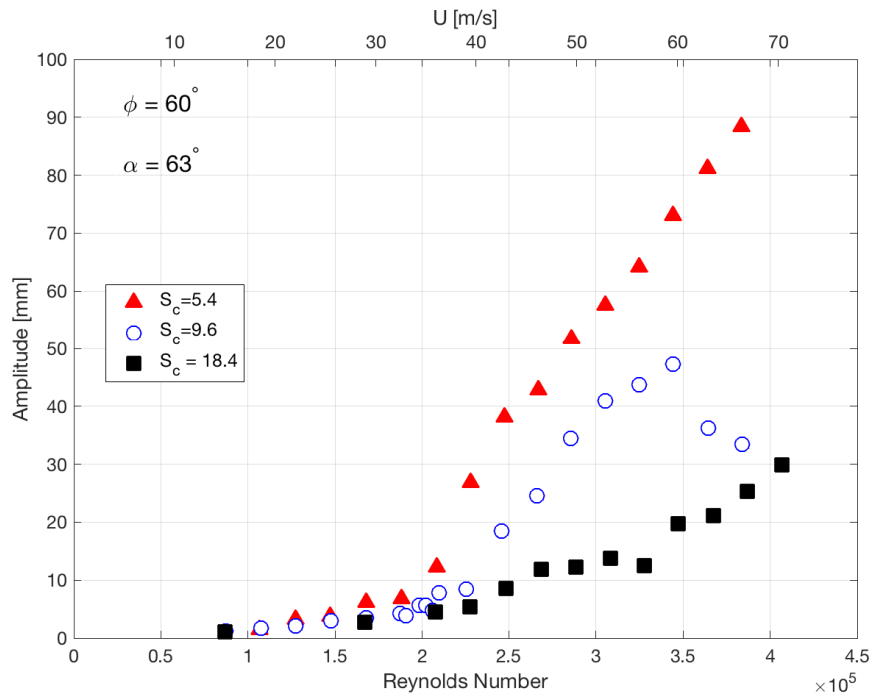
Figure 12 illustrates the relationship between the onset of the oscillations and the variations of the force coefficients with Reynolds number. The lift (C_L) and drag (C_D) coefficients of figure 12 are from the static tests on the same model in the same wind tunnel for the same angle of attack and same cable-wind angle.⁽²⁾



Source: FHWA.

Figure 12. Graphs. Variations of the (a) static lift coefficient, (b) static drag coefficient, and (c) dynamic response of cable model IR113E-HF as a function of Reynold's number for a cable-wind angle of 60 degrees and a Scruton number of 9.5.

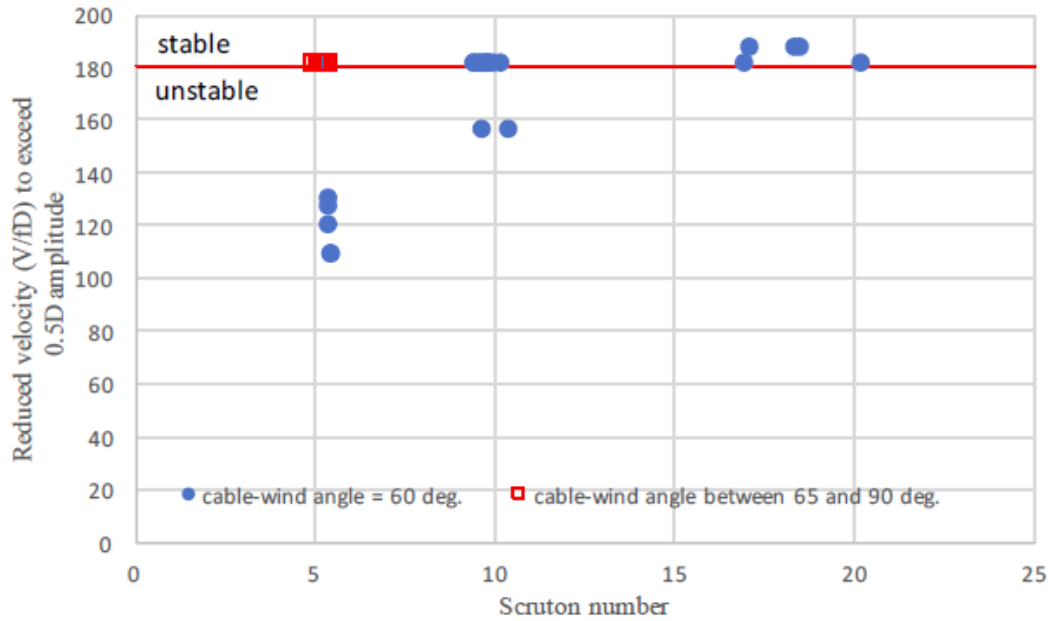
As opposed to what was observed for the flat-face reference model, an increase of Scruton number had a direct influence on the amplitude of the oscillations for cable model IR113E-HF at a cable-wind angle of 60 degrees. This influence is illustrated in figure 13. The angle of attack of the cable model was kept constant, and the damping of the dynamic rig was increased systematically for each run.



Source: FHWA.

Figure 13. Graph. Variations of the dynamic response of cable model IR113E-HF as a function of Reynolds number for a cable-wind angle of 60 degrees and three Scruton numbers.

As illustrated in figure 14, for all cable-wind angles that were tested above 60 degrees, no instabilities were observed for a Scruton number of 5. In figure 14, all points with a reduced velocity above 180 were stable. The influence of an increase of Scruton number on the oscillations is clear. Note that all cables of the Indian River Bridge have helical fillets and dampers.

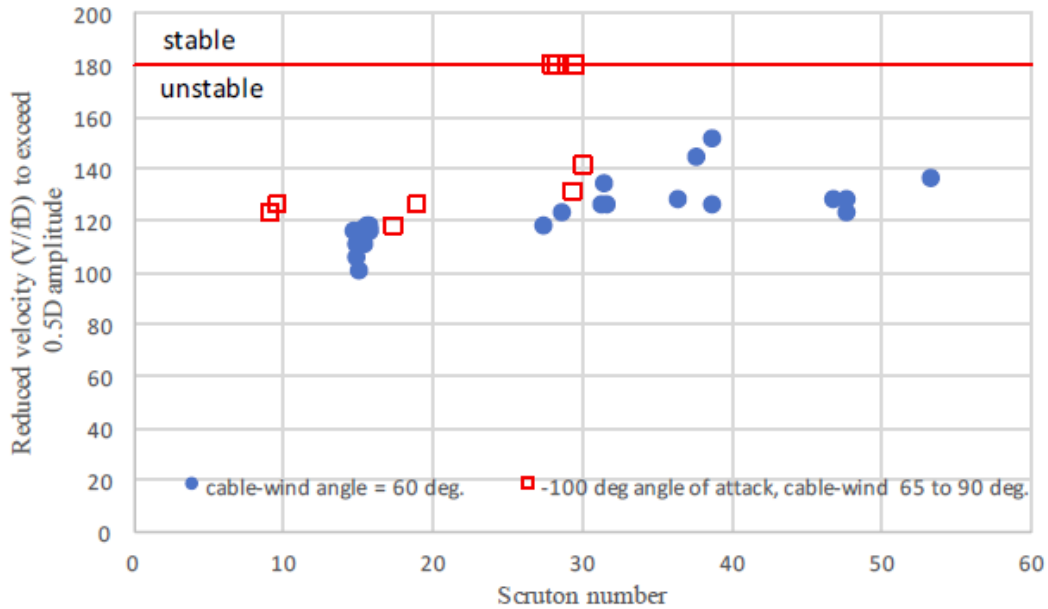


Source: FHWA.

Figure 14. Graph. Variations of the critical reduced velocity to exceed 0.5D amplitude as a function of Scruton number for the Indian River Bridge cable IR113E-HF model, with double helical fillets.

CABLE MODEL IR118E

The results for all tests with the Indian River Bridge cable IR118E (smooth surface) are presented in figure 15. Instabilities were observed for all angles of attack tested for the cable IR118E for a cable-wind angle of 60 degrees. Increasing the Scruton number had little influence on the amplitude of the response, even less influence than for the flat-face reference model. However, for cable-wind angle larger than 60 degrees, increasing damping had an influence on the response. The three points in figure 15 above a reduced velocity of 180 at Scruton numbers approaching 30 were stable for the entire range of Reynolds number studied.

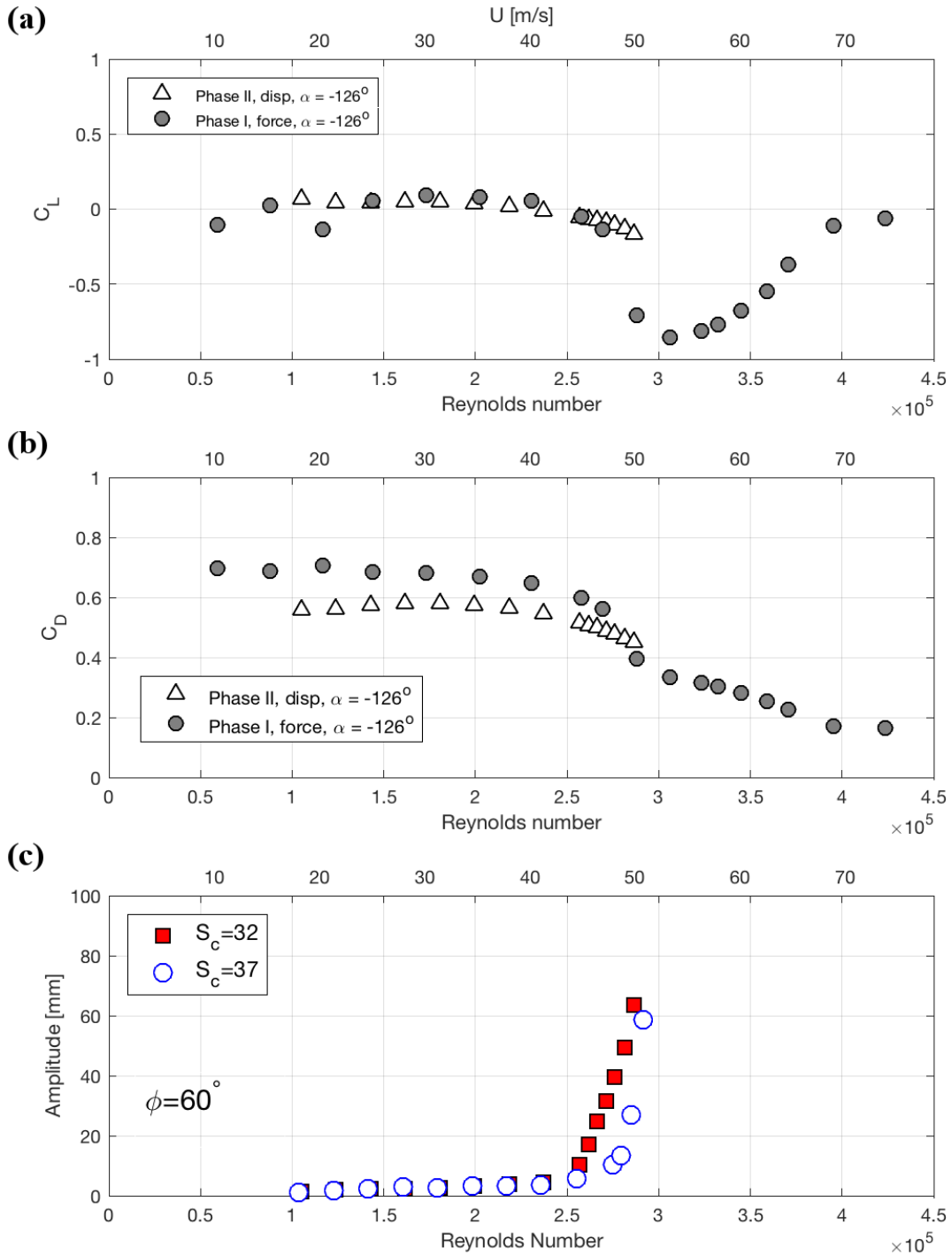


Source: FHWA.

Figure 15. Graph. Variations of the critical reduced velocity to exceed 0.5D amplitude as a function of Scruton number for the Indian River Bridge cable IR118E model, smooth surface.

The tests provided a clear indication that the aerodynamic phenomenon at the source of the excitation for this cable shape was different than for cable model IR113E-HF, even though all other parameters of the test were constant. As in figure 12, figure 16 illustrates the relationship between the force coefficients and the dynamic response as a function of Reynolds number. The onset of the excitation also appeared to be associated with a reduction of drag coefficient and an increase of lift coefficient, indicating the presence of a laminar separation bubble and the start of the TrBL1 regime. However, as the Reynolds number was increased, the vibrations grew rapidly in amplitude up to full instability. As shown in figure 16, this rapid growth in amplitude was for a Scruton number of 32, which is at least three times higher than the Scruton number of the majority of the stay cables for bridges in service. Increasing the Scruton number from 32 to 37 only delayed the onset of the instability by a few m/s.

Figure 16 shows not only the variations of the force coefficients with Reynolds number from the static tests but also the equivalent force coefficients calculated based on the mean displacements of the cable model in the dynamic rig.⁽²⁾ The stiffness of the dynamic suspension system in both the sway and heave modes was calibrated during the tests. The mean aerodynamic forces were deduced from the mean displacements and the stiffness of the rig. In general, the two sets of force coefficients were found to be in agreement, unless large oscillations were observed.



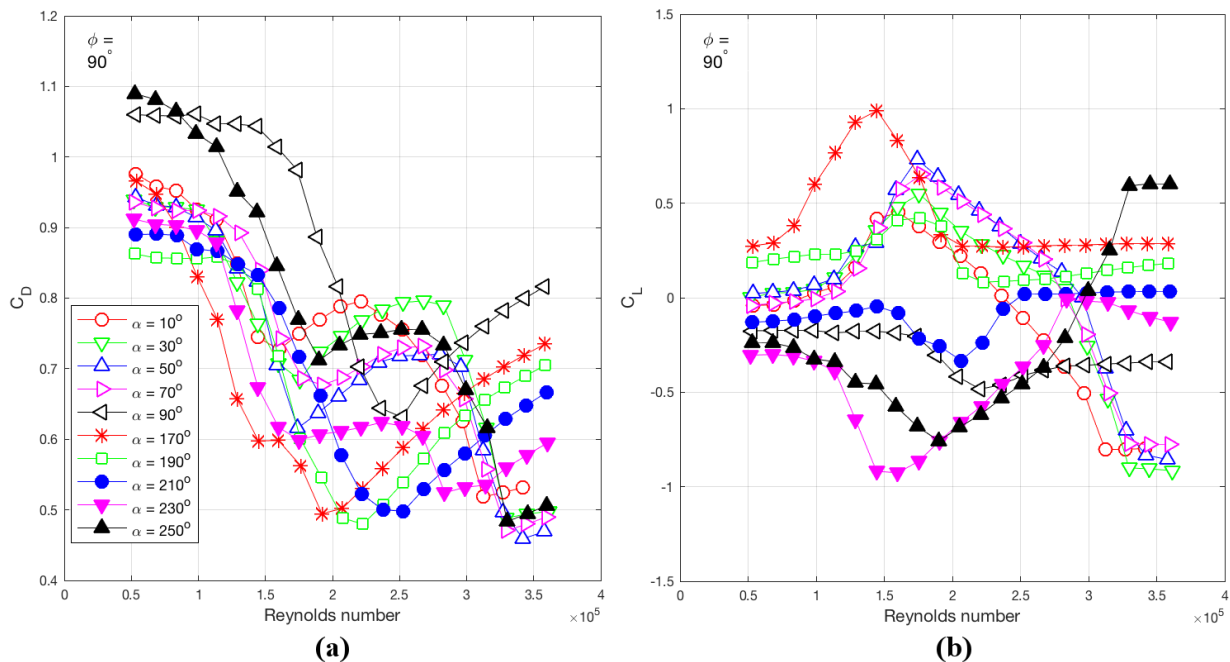
Source: FHWA.

Figure 16. Graphs. Variations of the (a) static lift coefficient, (b) static drag coefficient, and (c) dynamic response of cable model IR118E as a function of Reynolds number for a cable-wind angle of 60 degrees and two Scruton numbers.

CABLE MODEL WITH ICE/WET-SNOW ACCRETED SHAPE

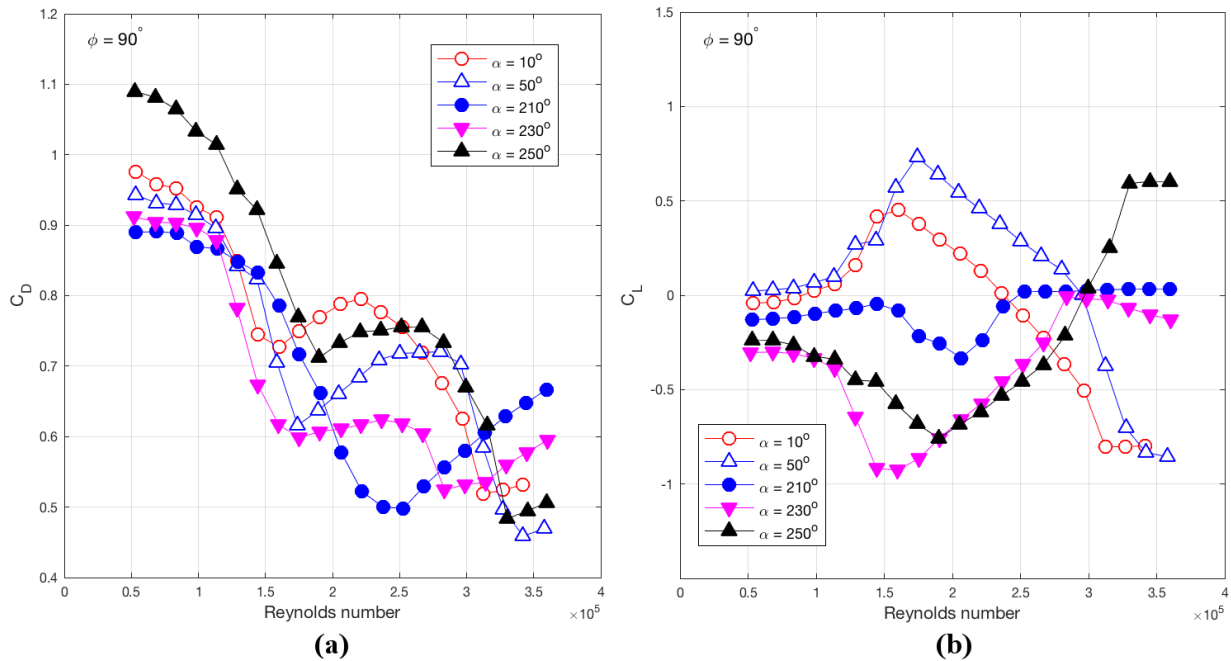
The simplified ice/wet-snow accreted shape was developed in the framework of this study. Before tests were performed in the dynamic rig, it was necessary to measure the static force coefficients as a function of Reynolds number and angle of attack. The dynamic rig was modified, replacing springs by rigid links connected to load cells at each extremity of the model. This modification allowed the static coefficients to be determined for the same testing conditions as for the dynamic tests, same model, same end conditions, and same flow conditions.

Figure 17 presents the static force coefficients for all angles of attack tested for a cable-wind angle of 90 degrees as a function of Reynolds number. As for the coefficients for the Indian River Bridge cables and the flat-face reference shape, the drag coefficients reduced significantly with Reynolds number, and large variations of lift coefficients with Reynolds number were also observed. The variations were found to be more pronounced for some of the angles of attack. By inspection of the coefficients, dynamic excitation was expected. Figure 18 and figure 19 present the coefficients for five of the angles of attack, selected for their adverse variations with Reynolds number, and a sketch of the cross section with a marking for these angles of attack, respectively. Adverse conditions with regard to aerodynamic stability were defined when a drop of the drag coefficient with Reynolds number was combined with a sharp variation of the lift coefficient due to change of Reynolds number or with angle of attack.



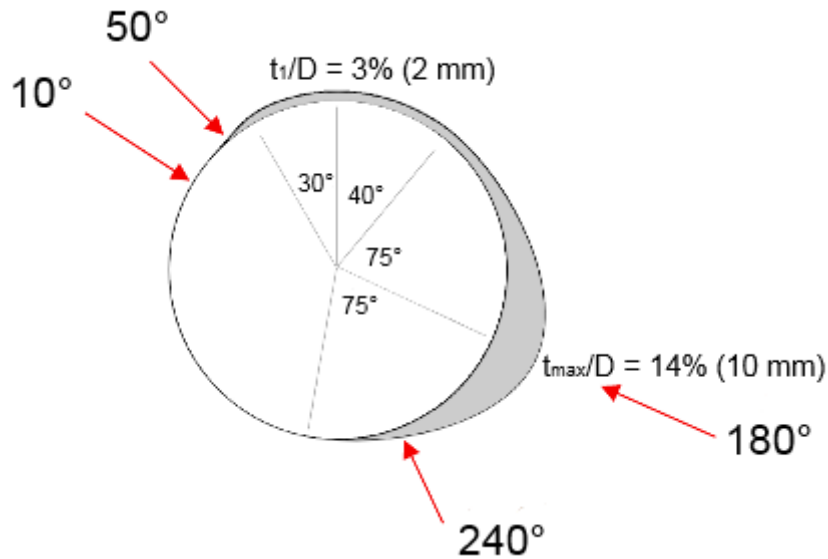
Source: FHWA.

Figure 17. Graphs. Variations of the (a) static drag coefficient and (b) static lift coefficient for the cable model with simplified ice/wet-snow accreted shape as a function of Reynolds number and angles of attack for a cable-wind angle of 90 degrees.



Source: FHWA.

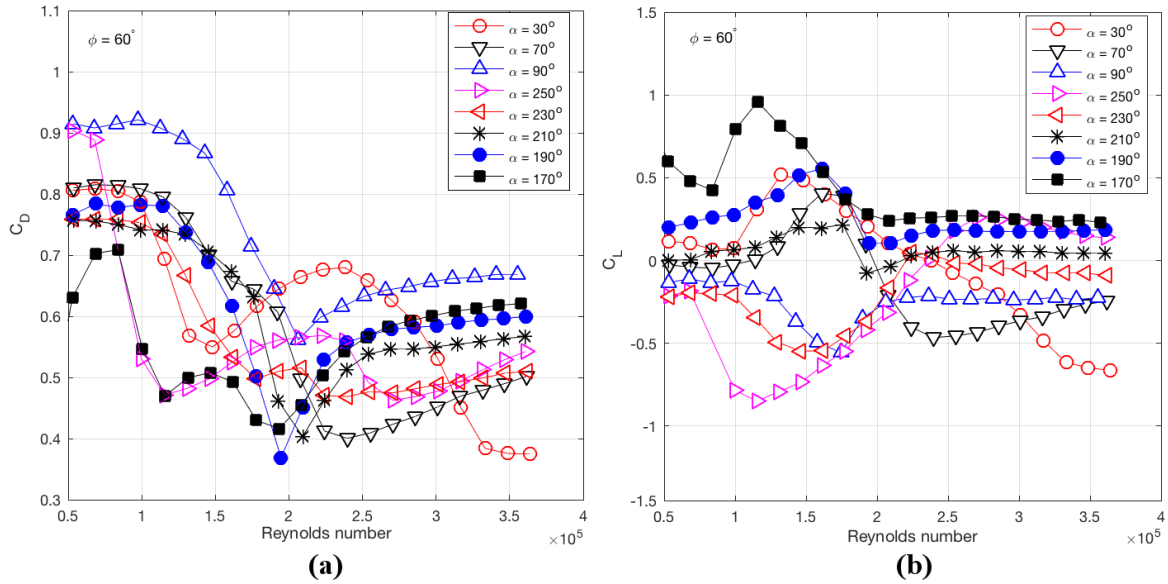
Figure 18. Graphs. Variations of the (a) drag coefficient and (b) lift coefficient for the cable model with simplified ice/wet-snow accreted shape as a function of Reynolds numbers for selected angles of attack for a cable-wind angle of 90 degrees.



Source: FHWA.

Figure 19. Illustration. Sketch of the simplified ice/wet-snow accreted shape marking the location of the angles of attack.

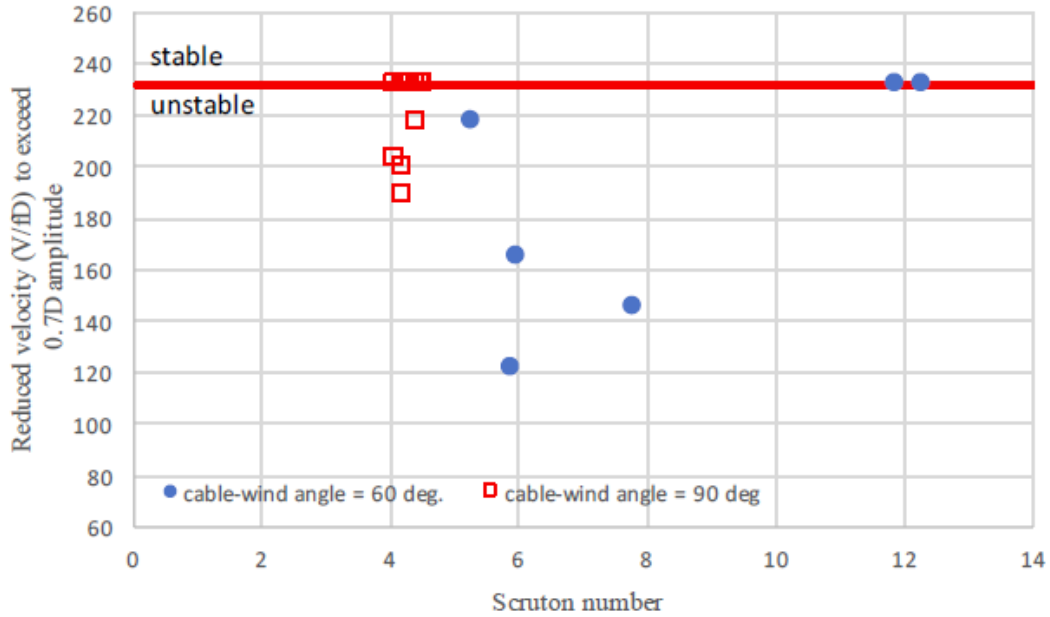
Figure 20 presents the static coefficients for a cable-wind angle of 60 degrees. The variations follow the same trends as for the cable-wind angle of 90 degrees.



Source: FHWA.

Figure 20. Graphs. Variations of the (a) static drag coefficient and (b) the static lift coefficient for the cable model with simplified ice/wet-snow accreted shape as a function of Reynolds numbers and angles of attack for a cable-wind angle of 60 degrees.

The results of the dynamic tests are presented in figure 21. As expected, instabilities were observed for cable-wind angles of both 90 and 60 degrees. For a cable-wind angle of 90 degrees, the angles of attack at which instabilities were observed at a Scruton number of 4.5 were 10, 230, 240, 250 and 320 degrees. The tests at 60 degrees exhibited generally stronger excitation; all angles of attack investigated (10, 30, 210, 214, 240, and 250 degrees) were unstable at a Scruton number below 8. For the IR113E cable with helical fillets an increase of Scruton number had a more important influence on the amplitude of the vibrations than for the flat-face reference shape. For the angles of attack investigated, a Scruton number of 12 was sufficient to mitigate the oscillations at a cable-wind angle of 60 degrees. Views of the cable model with the simplified ice/snow accreted shape (represented by white material in the figures) are presented in figure 22 through figure 24.



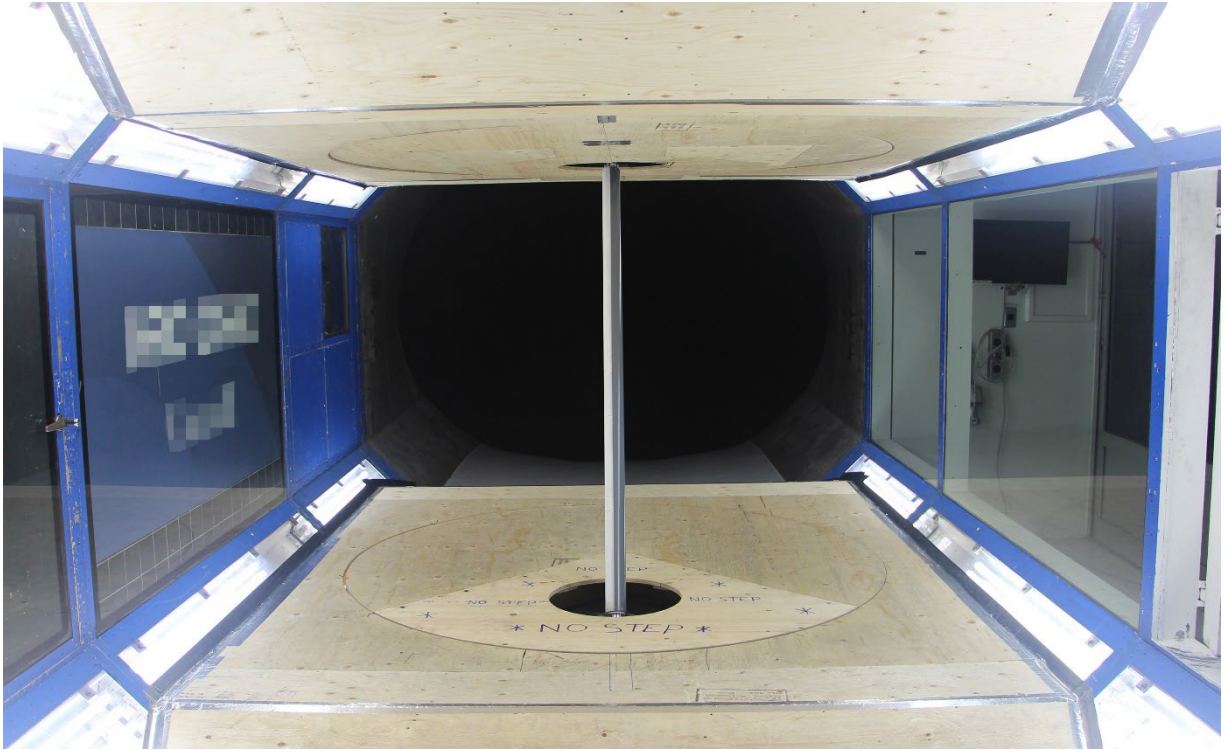
Source: FHWA.

Figure 21. Graph. Variations of the critical reduced velocity to exceed 0.7D amplitude as a function of Scruton number for the cable model with simplified ice/wet-snow accreted shape.



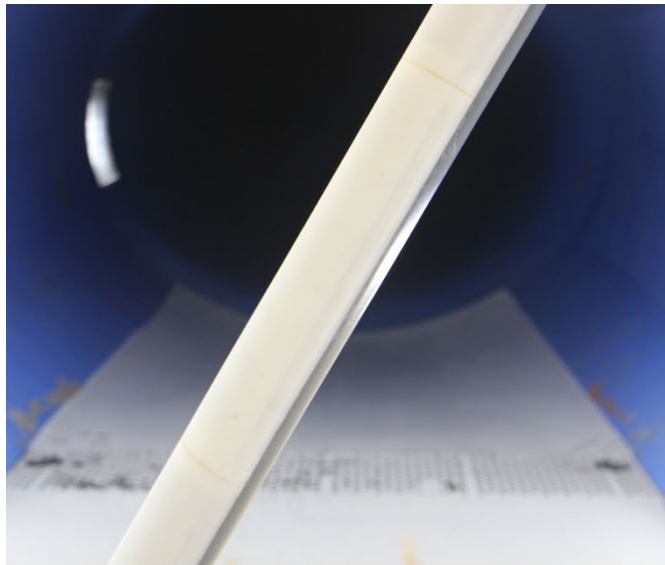
© 2017 RWDL.

Figure 22. Photo. View of the cable model with simplified ice/wet-snow accreted shape in the 2- by 3-m wind tunnel with a cable-wind angle equal to 90 degrees.



© 2017 RWDI.

Figure 23. Photo. View of the cable model with simplified ice/wet-snow accreted shape in the 2- by 3-m wind tunnel with a cable-wind angle equal to 60 degrees.



(a)



(b)

© 2017 RWDI.

Figure 24. Photos. (a) A side view and (b) a close-up view of the top end of the cable model with simplified ice/wet-snow accreted shape in the 2- by 3-m wind tunnel.

CONCLUSIONS OF THE EXPERIMENTS

Dynamic tests on replicas of cables for bridges in service revealed aerodynamic instabilities for all models for a variety of conditions. In general, inspection of the variations of the static coefficients with Reynolds number provided a good indication of the onset of the instability. However, for an inclination of 60 degrees at 0-degree yaw angle, large wind-induced oscillations were observed for most of the models and angles of attack investigated. These large oscillations could not be predicted solely based on the variations of the static force coefficients with Reynolds number and angles of attack. For these cases, increasing structural damping had only a small influence on the amplitude of the vibrations. However, for the cable model with helical fillets, increasing the Scruton number mitigated the vibrations as was first anticipated at the onset of the study.

CHAPTER 4. NUMERICAL SIMULATIONS

MOTIVATION

The full-scale measurements of HDPE cable casings on stay cables have shown deviations from the intended circular cross section. Analysis of wind-tunnel tests suggested that this anomaly may cause instabilities over a range of wind directions and angles of attack based on a linearized quasi-static model.^(2,7) Moreover, the estimated damping demands indicated the possibility that cable dampers may not be fully capable of mitigating wind-induced excitations on bridges built according to current design practice. Thus far, however, there is no strong evidence of unexplained and/or difficult-to-control cable vibrations on the existing bridges.

For reasons of practicality, numerical methods were used to replicate actual full-scale conditions. At a certain point, expanding the wind-tunnel tests by adding and varying additional conditions was not feasible. The researchers hoped that the quasi-static theory might be able to predict reasonably well the observed responses and extrapolate closer to full-scale conditions.

The linearized quasi-static aerodynamic damping model, in particular, allows for screening of potential quasi-static instabilities. However, the model does not allow for assessment of the self-limited features occasionally observed in classical galloping-like responses. Due to the rapid changes observed in the force coefficients with angle of attack, the cable may be expected to transition quickly from an unstable to a stable regime on the force coefficient curve once it begins to move. Therefore, extending the current linearized formulation to a nonlinear numerical method where these effects can be reproduced is necessary.

In this study, a comprehensive effort, including static and dynamic wind-tunnel tests, has been carried out to measure loads and simulate cable vibrations due to the shape variations. The Methodology section presents the ongoing research to evaluate, via testing and numerical response analyses, the conditions at full scale that may mitigate the vibrations, such as the influence of level of correlation of the cross-sectional shapes of the stay cables as a function of their length and wind turbulence.

METHODOLOGY

Natural Wind Effects

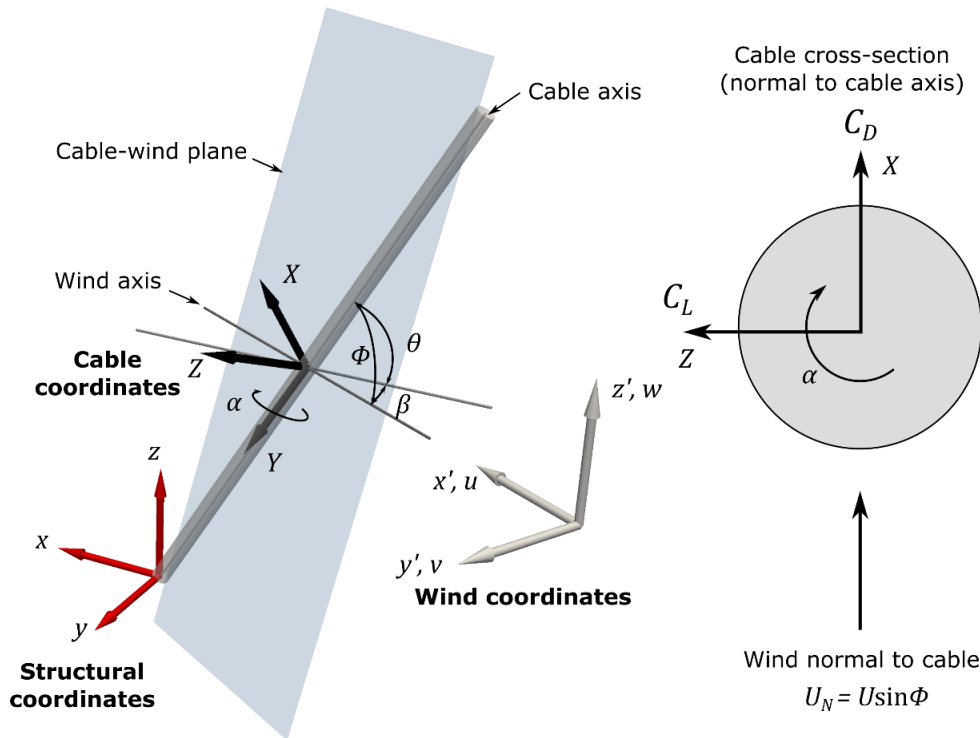
Previous research has shown that turbulence may have mitigative effects on stay-cable vibrations.⁽⁹⁾ Depending on the intensity and spatial properties, natural turbulence may have a significant impact on the cable response to wind. The turbulent fluctuations may cause transitions from subcritical to supercritical flow regimes (and vice versa). As the cable vibrates, its motions will superimpose with those caused by the turbulence fluctuations, further modifying the direct effects on the flow about the cable. These effects can be attributed to small length scale turbulent fluctuations (fluctuations at high frequencies that affect the flow in the boundary layer at the surface of the cable). In addition, the larger length scale variations will also affect the overall correlation of the fluctuating loads acting on long cables. The problem becomes extremely complex, given the cross sections are generally found nonsymmetric where even slight out-of-roundness (about 0.5–1 percent) was demonstrated to cause significant changes in the

aerodynamic properties. A sensitivity analysis of the wind-tunnel measurements showed that small changes in the mean angle of attack may cause a cross section to exhibit aerodynamic instabilities or to become stable. Therefore, variations of wind speed and direction over a few minutes until oscillations build up may also have a significant impact on the vibrating cables.

Coordinate Framework

Considering the 3D stay alignment, wind directionality, and structural response shown in figure 25, the following coordinate frameworks were selected to represent:

- The wind with coordinates x', y', z' and velocity vectors u, v, w .
- Structural coordinates x, y, z , and the locally aligned wind velocity vectors u_s, v_s, w_s .
- Cable loads with X, Y, Z (body system) and locally aligned wind velocity vectors U_l, V_l, W_l .



Source: FHWA.

Note: Shown are the definitions of the yaw angle β , the inclination angle θ , the cable-wind angle Φ , and the angle of attack α . The drag force lies in the cable-wind plane, and the lift force is normal to this plane.

Figure 25. Illustration. Sketch of the three coordinate systems: global (or structural), wind, and cable (or body).

The cable inclination angle from the horizontal plane is θ with wind direction angle β (yaw) yielding the effective cable-wind angle (Φ):

$$\Phi = \cos^{-1}(\cos \beta \cos \theta) \quad (2)$$

Due to wind turbulence and structural motions, these angles will vary in time where:

$$\beta(t) = -\tan^{-1}\left(\frac{v_s - \dot{y}}{u_s - \dot{x}}\right), \quad \theta(t) = \theta_0 + \tan^{-1}\left(\frac{w_s - \dot{z}}{u_s - \dot{x}}\right) \quad (3)$$

Where $\dot{x}, \dot{y}, \dot{z}$ are speed of structural response and θ_0 is the static cable inclination angle. For equation 3, wind is aligned in its mean direction, β_0 . The general transformation from structural to wind coordinates is:

$$\begin{Bmatrix} x' \\ y' \\ z' \end{Bmatrix} = \begin{bmatrix} \cos \beta_0 & -\sin \beta_0 & 0 \\ \sin \beta_0 & \cos \beta_0 & 0 \\ 0 & 0 & 1 \end{bmatrix} \begin{Bmatrix} x \\ y \\ z \end{Bmatrix} \quad (4)$$

The normalized transformation matrix $[T']$ from structural to body coordinates is:

$$[T'] = \begin{bmatrix} T_1 T_{11} & T_1 T_{12} & T_1 T_{13} \\ T_2 T_{21} & T_2 T_{22} & T_2 T_{23} \\ T_3 T_{31} & T_3 T_{32} & T_3 T_{33} \end{bmatrix}, \text{ with the norm } T_i = \|T_{i,j}\|^{-1}, j = 1..3., \quad (5)$$

$$\begin{bmatrix} T_{11} & T_{12} & T_{13} \\ T_{21} & T_{22} & T_{23} \\ T_{31} & T_{32} & T_{33} \end{bmatrix} = \begin{bmatrix} \cos \beta_0 \sin^2 \theta_0 & -\sin \beta_0 \cos^2 \theta_0 - \sin \beta_0 \sin^2 \theta_0 & \cos \beta_0 \sin \theta_0 \cos \theta_0 \\ \cos \theta_0 & 0 & -\sin \theta_0 \\ \sin \beta_0 \sin \theta_0 & \cos \beta_0 \sin \theta_0 & \sin \beta_0 \cos \theta_0 \end{bmatrix}$$

The transformations between structural and body coordinates performed as:

$$\begin{Bmatrix} X \\ Y \\ Z \end{Bmatrix} = [T'] \begin{Bmatrix} x \\ y \\ z \end{Bmatrix} \quad (6)$$

and for wind from global to local coordinates via:

$$\begin{Bmatrix} U \\ V \\ W \end{Bmatrix} = [T'] \begin{bmatrix} \cos \beta_0 & -\sin \beta_0 & 0 \\ \sin \beta_0 & \cos \beta_0 & 0 \\ 0 & 0 & 1 \end{bmatrix}^T \begin{Bmatrix} u \\ v \\ w \end{Bmatrix} \quad (7)$$

The quasi-static forces are computed from:

$$\begin{Bmatrix} F_x \\ F_y \\ F_z \end{Bmatrix} = \frac{1}{2} \rho (u - \dot{x})^2 d \begin{bmatrix} \cos \alpha & 0 & -\sin \alpha \\ 0 & 1 & 0 \\ \sin \alpha & 0 & \cos \alpha \end{bmatrix} \begin{Bmatrix} C_D(\alpha, Re, \Phi) \\ C_A(\alpha, Re, \Phi) \\ C_L(\alpha, Re, \Phi) \end{Bmatrix} \quad (8)$$

Where C_A is the along-cable static force coefficient and $u(t) = \bar{u} + u'(t)$, where $u'(t)$ is the fluctuating component. Given the cross section is not symmetric about its longitudinal axis Y , the forces will generally depend on the angle of local wind attack, as well on the instantaneous velocity (comprising structural motions) and effective wind angle reflecting the variations of both β and θ .

Similar to previous studies the angle of local wind attack is calculated from:^(9,10)

$$\alpha(t) = \frac{W(t) - \dot{Z}}{U(t) - \dot{X}} \quad (9)$$

Where $\alpha(t)$ is the instantaneous variation of angle of wind attack. This angle of attack is measured off the drag axis X . The Reynolds number is calculated as:

$$Re = \frac{(u - \dot{x})D}{\nu} \quad (10)$$

Where ν is air kinematic viscosity. Due to its insignificant effect (actual wind speed fluctuations much higher compared to structural speeds) the structural motions term \dot{x} is omitted. All force coefficients are derived based on the effective wind direction Φ . Likewise, the reference wind velocity \bar{u} is the speed used for force coefficient normalization, thus, the mean speed in the wind coordinate system (or wind tunnel).

Linear Quasi-Static Formulation

The potential for dry cable galloping has been assessed using a linearization of the quasi-static forces by Macdonald and Larose.^(7,11,12) In this linearized quasi-static formulation, the aerodynamic damping is expected to be a function of angle of attack α , the cable-wind angle Φ , and the Reynolds number Re :

$$\begin{aligned}
\zeta_{aero} = \frac{\mu Re}{4m\omega_n} & \left\{ \cos \alpha \left[C_D \left(2 \sin \Phi \cos \alpha + \frac{\sin^2 \alpha}{\cos \alpha \sin \Phi} \right) + \frac{\partial C_D}{\partial Re} Re \sin \Phi \cos \alpha \right. \right. \\
& \left. \left. + \frac{\partial C_D}{\partial \Phi} \cos \Phi \cos \alpha - \frac{\partial C_D}{\partial \alpha_0} \frac{\sin \alpha}{\sin \Phi} \right] \right. \\
& \left. - \sin \alpha \left[C_L \left(2 \sin \Phi \cos \alpha - \frac{\cos \alpha}{\sin \Phi} \right) + \frac{\partial C_L}{\partial Re} Re \sin \Phi \cos \alpha \right. \right. \\
& \left. \left. + \frac{\partial C_L}{\partial \Phi} \cos \Phi \cos \alpha - \frac{\partial C_L}{\partial \alpha_0} \frac{\sin \alpha}{\sin \Phi} \right] \right\}
\end{aligned} \tag{11}$$

Where:

μ = air dynamic viscosity.

ζ_{aero} = aerodynamic damping (ratio of critical).

ω_n = circular frequency of the nth cable mode.

It should be noted that the angle of attack used in equation 11 has an inherent implication about the direction of body motion. For along-wind motions the value for the angle of attack is $\alpha = 0$ degrees, and for across-wind motions it should be $\alpha = 90$ degrees. However, as indicated by the “0” subscript, the values for the change in drag and lift with angle of attack should be calculated about the 0-degree α position (i.e., the along-wind axis in figure 25). Therefore, for a yaw angle of 0 degrees, the predicted damping in the structural y -direction reduces to a form similar to the familiar Den Hartog expression for galloping:⁽¹³⁾

$$\zeta_{aero} = \frac{\mu Re}{4m\omega_n} \left(C_D + \frac{\partial C_L}{\partial \alpha_0} \right) \frac{1}{\sin \Phi} \tag{12}$$

Nonlinear Quasi-Static Formulation

Equations 2, 3, 9, and 10 are all functions of time and can be computed at each time step of a numerical simulation. Based on the instantaneous values of angle of attack α , the cable-wind angle Φ , and the Reynolds number Re , the instantaneous force coefficients are computed at each time step based on interpolations from the measured values. The computed $C_D(t) = C_D(\alpha, Re, \Phi)$ and $C_L(t) = C_L(\alpha, Re, \Phi)$ are substituted into equation 8 to obtain the instantaneous force per unit length in the cable coordinate system. These cable-oriented forces are rotated back to the structural coordinate system following the transformation of equation 6, and the system of ordinary differential equations is solved at each time step using the generalized multidegree of freedom (MDOF) state-space representation, e.g.⁽¹⁴⁾

$$\begin{bmatrix} -C^* & -K^* \\ I & 0 \end{bmatrix} \begin{Bmatrix} \dot{q}(t) \\ q(t) \end{Bmatrix} = \begin{Bmatrix} \ddot{q}(t) \\ \dot{q}(t) \end{Bmatrix} - \begin{Bmatrix} F^*(t) \\ 0 \end{Bmatrix} \tag{13}$$

Where:

q, \dot{q}, \ddot{q} = generalized responses of the cable.
 F^* = the generalized response-dependent forces.
 I = the identity matrix.
 C^* = the generalized (diagonal) damping matrix.
 K^* = the generalized (diagonal) stiffness matrix.

No modifications to the damping or stiffness matrices are performed to account for the self-excited forces as these forces are implicitly calculated by using the instantaneous values of angle of attack α , the cable-wind angle Φ , and the Reynolds number Re . The time step in the simulation was set to 0.005 s, and the simulation was computed until a steady-state motion was achieved. Given the nonlinear nature of the loading, at every time step an iteration procedure based on response convergence has been applied where the solution above is carried out in a MDOF framework, which allows for the flexibility to numerically model more closely the assembly process of actual stay cables.

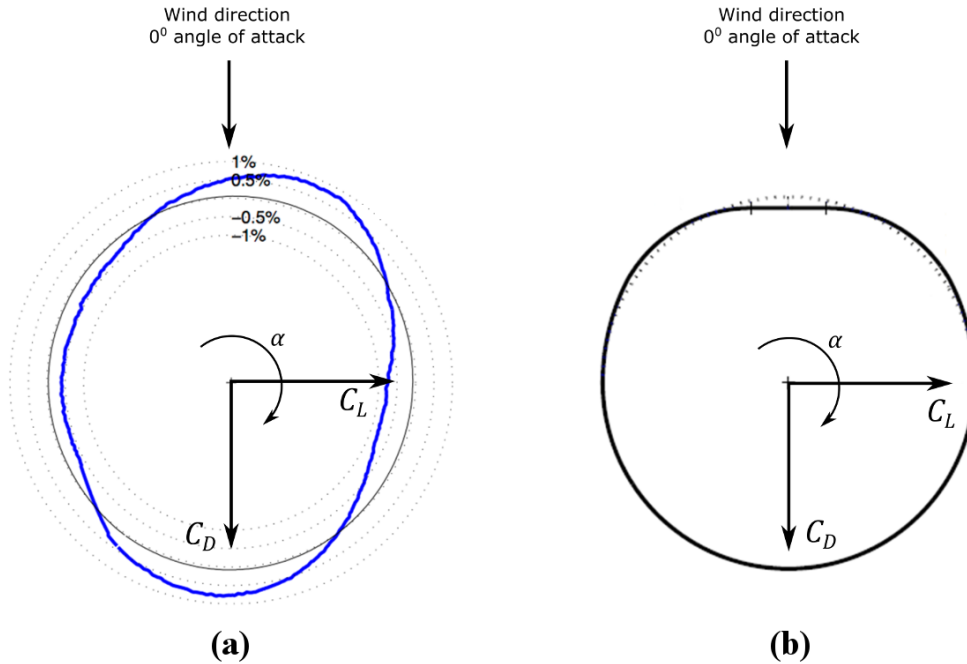
As previously discussed, it has been observed that cable cross sections are not perfectly circular, and the aerodynamic forces have a strong dependence on the particular cross-sectional shape. Stay cables are sheathed with HDPE in a segmented fashion. Thus, even if each cross section was the same from one segment to the next, it is unlikely that the initial angle of attack α is the same for each segment. In addition to modeling the assembly process of stay cables, the proposed numerical methodology can also incorporate the effect of turbulence. To simulate the effects of turbulence, one can either use available site measurement data or synthesize turbulent flows through autoregression or other available numerical techniques.¹

EXPERIMENTS

There are two sets of experimental data used in the current study. The first set of wind tunnel experiments were performed to measure the drag and lift coefficients over a wide range of values of angle of attack α , cable-wind angles Φ , and Reynolds numbers Re .⁽²⁾ These data are interpolated so that the instantaneous drag and lift coefficients can be obtained based on the instantaneous values of each variable. This 3D interpolation “volume” forms the input required for the numerical simulations.

The second experiment set, described in chapter 3 of this report, provided free-vibration response data to compare with the performance of the proposed numerical simulation methodology. Figure 26 shows the cases considered in the current study.

¹ RWDI Reference BR01-2007, “Numerical Simulation of Wind Turbulence”, March 7, 2007.



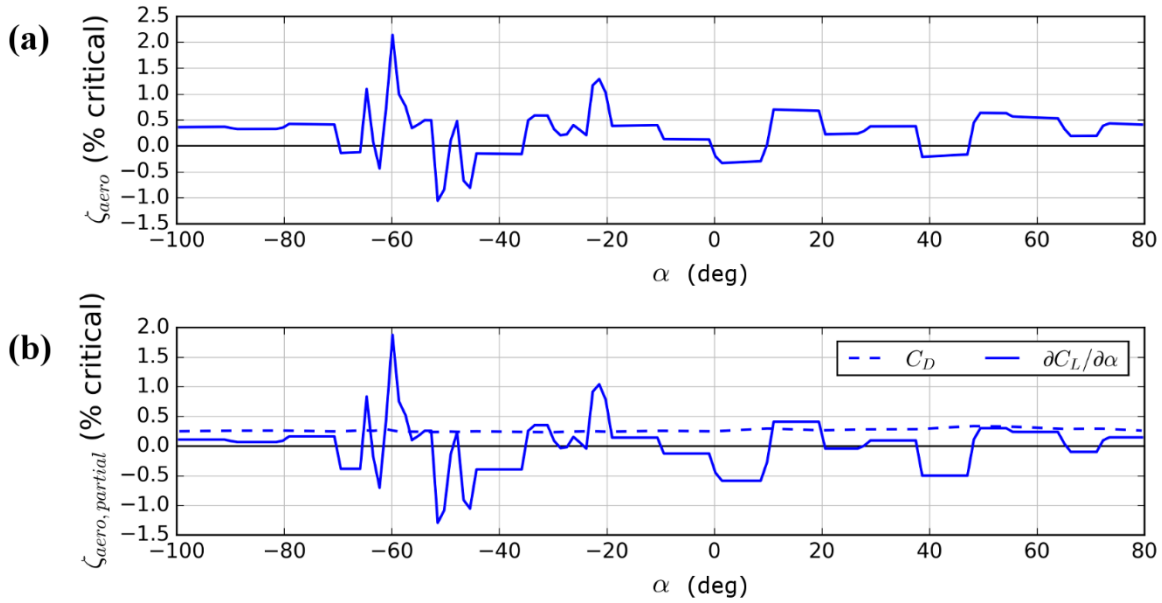
Source: FHWA.

Figure 26. Illustration. Analyzed cross-section shapes: (a) IR113E-HF (exaggerated by a factor of 10) and (b) the flat-face symmetric cable.

RESULTS

Aerodynamic Damping

Each term in equation 11 has been computed for the case of IR113E-HF at a yaw angle of 0 degrees, a cable inclination of 60 degrees, and $Re = 2.4 \times 10^5$. With most terms, identically zero for this case, it is clear from figure 27 that the dominant term providing negative aerodynamic damping is the rate-of-change of lift with the angle of attack, where the drag term provides positive aerodynamic damping. It is observed that the variation in predicted damping with angle of attack is not smooth but changes abruptly over small changes in the angle of attack. Based on the observations from figure 27, the initial angle of attack producing the most negative aerodynamic damping in this case was near -51 degrees.



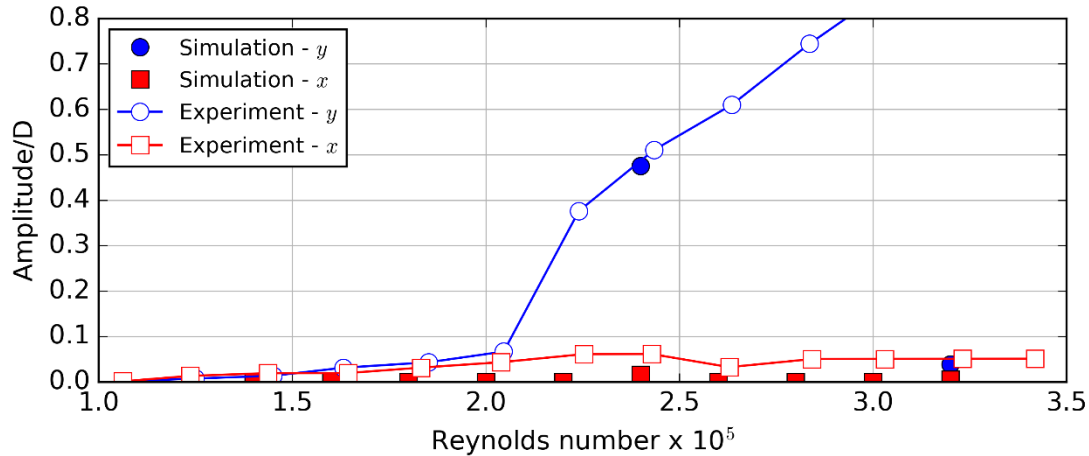
Source: FHWA.

Note: The yaw and inclination angles are set to 0 and 60 degrees, respectively, with $Re = 2.4 \times 10^5$. The legend entries keep only the force coefficient portion of each term.

Figure 27. Graphs. Across-wind aerodynamic damping predicted by equation 11 for (a) the total aerodynamic damping and (b) the contribution of each term.

Indian River Bridge IR113E-HF at 0-Degree Yaw

Numerical simulations have been performed based on the approach described in the chapter 4 Methodology section. The worst-case angle of attack $\alpha = -51$ degrees for IR113E-HF as estimated from equation 11 has been simulated numerically as tested in the wind tunnel. The results are shown in figure 28 for a Scruton number equal to 5.3. In general, the numerical simulations did not predict any steady-state motion of the cable, whereas significant responses were clearly observed in the wind-tunnel tests.



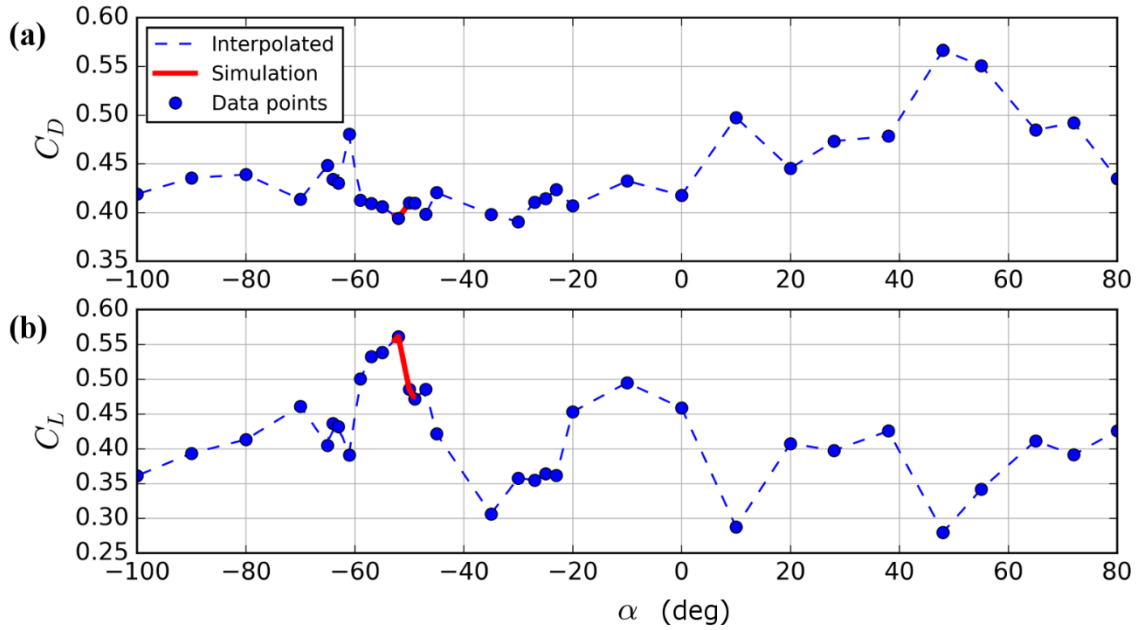
Source: FHWA.

Note: The x -direction is along-wind and the y -direction is across-wind.

Figure 28. Graph. Numerical simulations versus experimental results for Indian River Bridge cable IR113E-HF with $Sc = 5.3$ and yaw and inclination angles of 0 and 60 degrees, respectively.

However, good agreement is found for a Reynolds number of 2.4×10^5 . It should be noted that the numerical simulations were performed with and without initial excitations of the cable, and the same steady-state results were achieved regardless of the initial excitation.

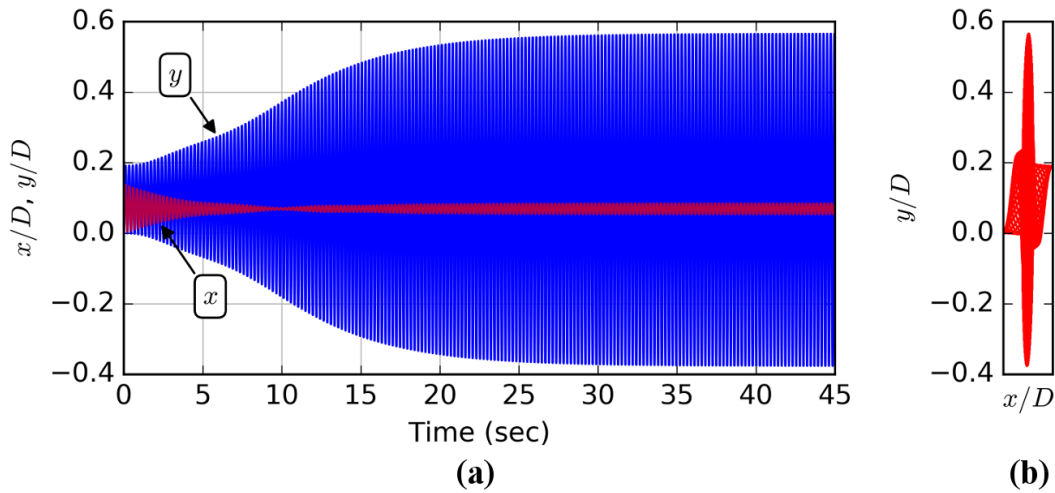
As shown in the 2021 FHWA report, the drag and lift coefficients change rapidly with both Reynolds number and angle of attack for this case.⁽²⁾ The drag and lift coefficients as a function of angle of attack are presented in figure 29 for $Re = 2.4 \times 10^5$. It should be noted that the “data points” in figure 29 themselves are a result of Reynolds number interpolations. The force coefficient data were obtained by fixing the angle of attack and increasing the wind speed to cover a wide range of Reynolds number. Therefore, to extract data at a particular Reynolds number, an interpolation from these runs was required.



Source: FHWA.

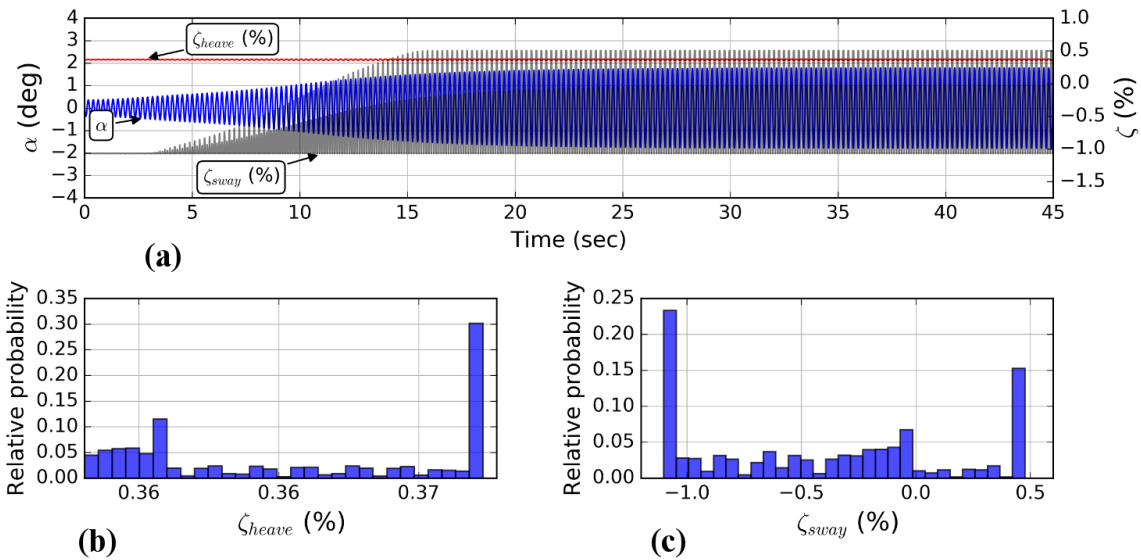
Figure 29. Graphs. Comparison of numerical simulations to interpolated data for (a) drag and (b) lift coefficients for IR113E-HF for $\Phi = 60$ degrees and $Re = 2.4 \times 10^5$.

As observed from figure 29, the aerodynamic excitation grows over the portion of the lift curve where there is a significant negative slope. However, as soon as the instantaneous angle of attack (equation 9) exceeds this negative slope region, the aerodynamic forces return to a stabilizing regime. Thus, the shape of the force coefficient curves leads to a steady-state response, as shown in figure 30. As a further illustration, the linear estimate of aerodynamic damping, in equation 11 has been calculated at each instant of time in figure 31.



Source: FHWA.

Figure 30. Graphs. Time series of response for IR113E-HF at $\Phi = 60$ degrees and $Re = 2.4 \times 10^5$ with $Sc = 5.3$ where (a) is response plotted against time and (b) is y -response plotted against x -response with the same scale on both axes.



Source: FHWA.

Note: Relative probability histograms are calculated based on the linear approximation shown in equation 11 at each instant of time corresponding to the instantaneous parameters α , Φ , and Re .

Figure 31. Graphs. The (a) aerodynamic damping (right axis) plotted with angle of attack α (left axis) for IR113E-HF at $\Phi = 60$ degrees and $Re = 2.4 \times 10^5$ with $Sc = 5.3$, combined with the relative probability (counts per bin/total) of the damping in (b) heave and (c) sway.

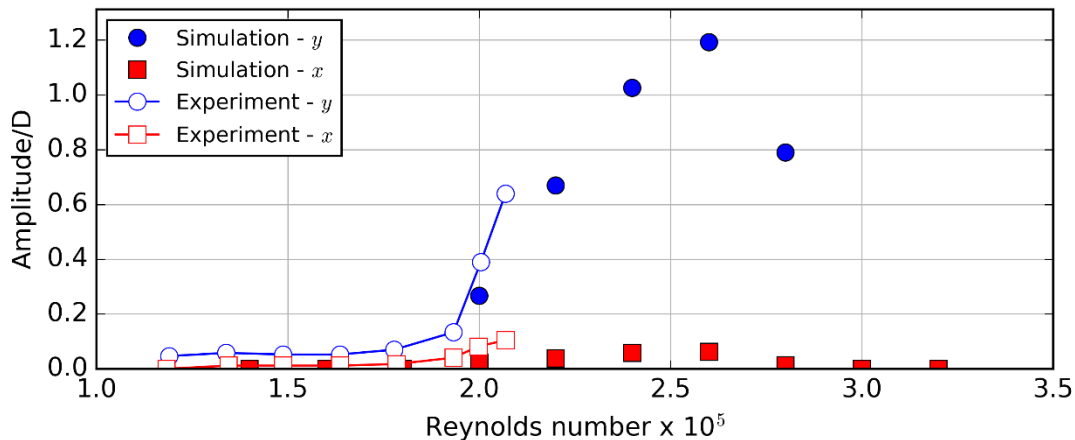
This estimate is based on the instantaneous drag and lift coefficients and their slopes determined from the angle of attack α , cable-wind angle Φ , and Re .

The structural damping in this case was approximately 0.6 percent of critical damping. Figure 31 shows that the negative aerodynamic damping exceeds this basic structural damping at some angles of attack but returns to positive values at sufficiently negative angles of attack (as measured from the initial angle of attack).

Wind-tunnel data are also available for a case with increased Scruton number ($Sc = 9.7$). For this case, motions up to approximately 0.5 times the cable diameter were observed in the wind tunnel but could not be recreated for any Re in the numerical simulations. Therefore, it appears these motions might be a different phenomenon causing the instability, which cannot be simulated by the quasi-static numerical model.

Flat-Face Reference Shape Cable at 0-Degree Yaw

The free vibration wind-tunnel data indicate that the flat-face cable model will be unstable for $Re > 2 \times 10^5$ with initial angles of attack of ± 20 degrees (due to symmetry). Numerical simulations have been carried out for this case and comparisons with the wind-tunnel data are shown in figure 32. There is reasonable agreement observed between the numerical predictions and the wind-tunnel results for this case acknowledging that the wind-tunnel test had to be stopped due to large cable motions.



Source: FHWA.

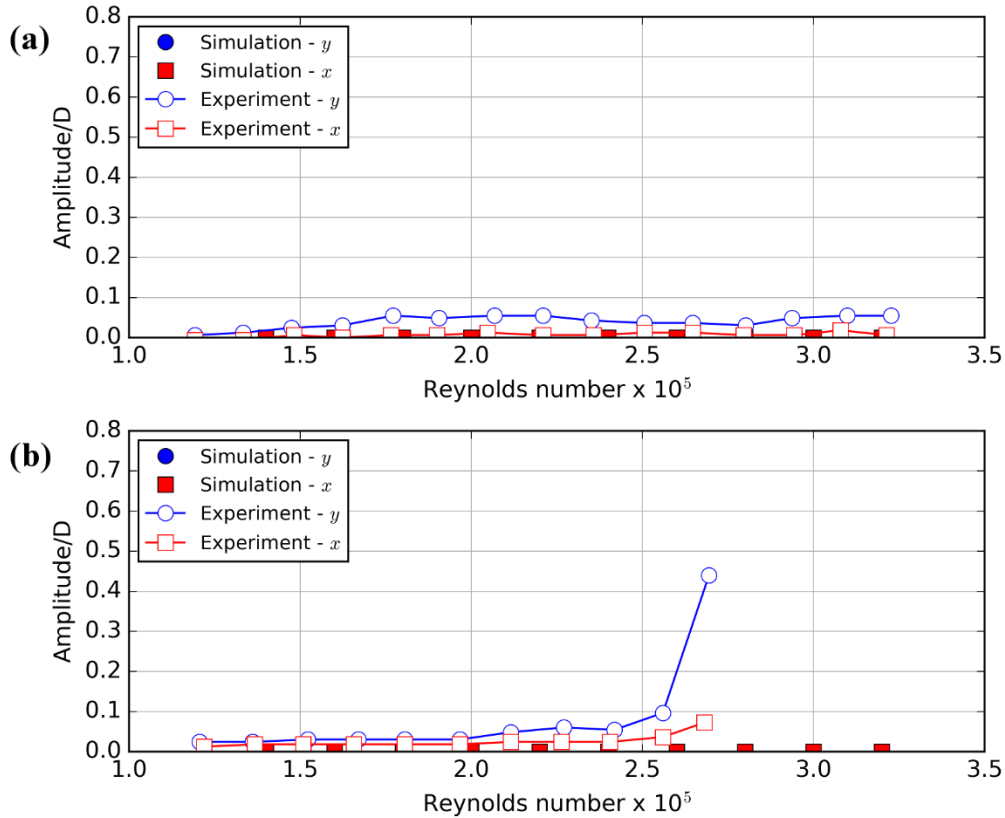
Note: The x -direction is along-wind and the y -direction is across-wind.

Figure 32. Graph. Comparison of numerical predictions to experimental results for the flat-face cable with $Sc=17.5$ with initial angle of attack set to 20 degrees, and with yaw and inclination angles set to 0 and 60 degrees, respectively.

Flat-Face Cable Model with Spatial Variation

Following the initial tests and simulations of the flat face cable model with a constant angle of attack, wind-tunnel tests were performed with spatial variation of the initial angle of attack. The cable was divided into three segments of the same cross section such that each segment could have a different initial angle of attack. Spatial variation was modeled numerically using multiple nodes along the cable length. Simulations have been performed for two of these cases as shown in figure 33. In figure 33(a) the lowest portion of the cable was set to 80 degrees with the middle

and top parts both set to an initial angle of attack of 10 degrees. In the 2015 static tests, it was observed that the flat face cable model had adverse force coefficients at an angle of attack of 80 degrees. For figure 33(b), the bottom and top of the section were set to an initial angle of attack of 80 degrees with the middle portion set to 30 degrees.



Source: FHWA.

Note: The x-direction is along-wind and the y-direction is across-wind.

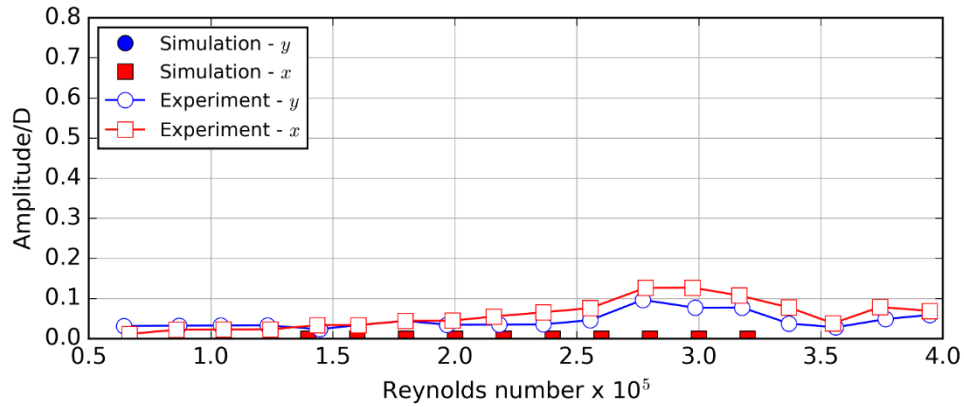
Figure 33. Graphs. Comparison of numerical simulations to experimental results for the flat-face cable of three rotated sections with initial angle of attack of (a) 80, 10, and 10 degrees and (b) 80, 30, and 80 degrees with $Sc = 20$ and yaw and inclinations angles set to 0 and 60 degrees, respectively.

In the first case (figure 33(a)), no motion was observed in either the wind-tunnel experiments or the numerical simulations. In the second case (figure 33(b)), large amplitude motions still persisted in the wind tunnel at $Re > 2.7 \times 10^5$; however, no responses were predicted numerically.

Indian River Bridge IR113E-HF at 60-Degree Yaw

The numerical framework here combined with the extensive database of force coefficients permitted simulations for a wide range of yaw angles in addition to variations in the initial angle of attack. Wind-tunnel tests were also performed over a range of yaw angles; however, no significant responses indicative of an aerodynamic instability were observed.

This observation is consistent with the numerical simulations where no quasi-static instability was observed. An example of these simulations and wind-tunnel measurements is shown in figure 34.



Source: FHWA.

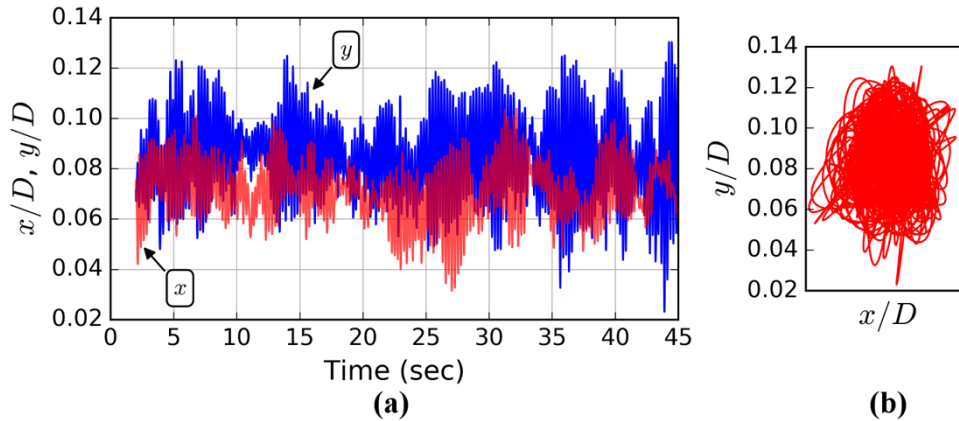
Note: The x -direction is along-wind, and the y -direction is across-wind.

Figure 34. Graph. Comparison of numerical simulations to experimental results of IR113E-HF with $Sc = 5.2$ with initial angle of attack set to -55 degrees, and yaw and inclination angles set to 60 and 60 degrees, respectively.

Simulations for IR113E-HF at 0-Degree Yaw with Turbulence

The case considered earlier for IR113-HF at 0-degree yaw and $Re = 2.4 \times 10^5$ (figure 28) where good agreement was observed with the wind-tunnel tests has been subjected to numerically generated turbulence with turbulence intensity $I_u = \sigma_u/\bar{u}$ of approximately 5 percent. The turbulence generally follows the shape of the von Kármán spectra for each wind direction.

As observed in figure 35, the previously predicted instability in smooth flow was suppressed by turbulence. The rapid variation of instantaneous angle of attack, Re , and cable-wind angle due to the approaching turbulent flow implies that little time is spent at the unstable portion of the force coefficient curve to allow an instability growth; the typical buffeting response is predicted instead.



Source: FHWA.

Figure 35. Graph. Time series of response for IR113E-HF at $\Phi = 60$ degrees and $Re = 2.4 \times 10^5$ with $Sc = 5.3$ and $I_u \approx 5$ percent where (a) is response plotted against time and (b) is y -response plotted against x -response with the same scale on both axes.

DISCUSSIONS AND CONCLUSIONS

The 3D nonlinear quasi-static modeling approach showed good agreement to what was observed in the wind-tunnel experiments for cables inclined in the wind direction. In other cases, especially for a cable-wind angle of 60 degrees, the comparisons showed that the proposed aerodynamic model cannot explain the wind-tunnel results. The likely reasons for these discrepancies are:

- Lack of details in the static force coefficients data: There were trends of very sharp gradients in the transitions from stable to unstable regions and vice versa requiring detailed knowledge of the force coefficients over the three-parameter space: angle of attack, cable-wind angle, and Reynolds number. Even though very fine increments of angle of attack (e.g., approximately 1 degree) had been measured in some cases, it was a practical challenge to sample the entire parameter space experimentally.
- Different aerodynamic phenomena caused the instabilities: Some of the large amplitude vibrations found during the test could not be predicted and/or did not follow the general expectations based on quasi-static theory. For example, physical tests with increased damping in the wind tunnel had shown a limited influence of the added damping on the oscillations, even at high levels of Scruton number. These observations indicated that another aerodynamic excitation mechanism (perhaps stiffness driven) might play a significant role in the observed responses. Identifying and modeling aerodynamic phenomena outside of those described by quasi-static theory was beyond the scope of the current research program.

Numerical tests showed that turbulence might be able to suppress the vibrations predicted in smooth flow.

APPENDIX. TEST LOGS

Test logs of the dynamic tests conducted for this study are provided in table 3.

Table 3. Test log data for test number 1003.

Run Num	Points	Tare Run	Inclination Angle (Degrees)	Cable Axis Rotation (Degrees)	Turntable Yaw (Degrees)	Phi (Degrees)	Sway (Hz)	Heave (Hz)	Sway (Percent)	Heave (Percent)	Cable Name	Case Type
31	1	30	60	0	0	60	4.39	4354	0.27	0.27	Flat-face	Dynamic
33	14	32	60	0	0	60	4.39	4354	0.27	0.27	Flat-face	Dynamic
56	7	54	60	10	0	60	4.41	4.25	0.32	0.30	Flat-face	Dynamic
57	8	54	60	10	0	60	4.41	4.25	0.32	0.30	Flat-face	Dynamic
60	12	58	60	20	0	60	4.41	4.24	0.33	0.30	Flat-face	Dynamic
63	13	61	60	30	0	60	4.42	4.24	0.35	0.30	Flat-face	Dynamic
66	14	64	60	40	0	60	4.41	4.24	0.32	0.30	Flat-face	Dynamic
69	14	67	60	60	0	60	4.42	4.24	0.35	0.30	Flat-face	Dynamic
72	15	70	60	80	0	60	4.42	4.24	0.32	0.30	Flat-face	Dynamic
75	16	73	60	90	0	60	4.41	4.24	0.32	0.29	Flat-face	Dynamic
78	12	76	60	100	0	60	4.41	4.24	0.35	0.30	Flat-face	Dynamic
81	18	79	60	120	0	60	4.41	4.25	0.32	0.30	Flat-face	Dynamic
87	14	84	60	0	0	60	4.41	4.25	0.42	0.35	Flat-face	Dynamic
92	15	90	60	0	0	60	4.41	4.24	0.72	0.70	Flat-face	Dynamic
96	15	94	60	0	0	60	4.41	4.24	0.72	0.68	Flat-face	Dynamic
99	16	97	60	20	0	60	4.41	4.24	0.74	0.69	Flat-face	Dynamic
102	14	100	60	30	0	60	4.41	4.24	0.74	0.70	Flat-face	Dynamic
105	15	103	60	40	0	60	4.41	4.24	0.74	0.70	Flat-face	Dynamic
108	16	106	60	60	0	60	4.41	4.24	0.80	0.70	Flat-face	Dynamic
111	16	109	60	80	0	60	4.41	4.24	0.75	0.69	Flat-face	Dynamic
114	12	112	60	100	0	60	4.41	4.24	0.78	0.68	Flat-face	Dynamic
117	18	115	60	120	0	60	4.41	4.24	0.78	0.70	Flat-face	Dynamic
120	19	118	60	120	0	60	4.40	4.23	1.45	1.32	Flat-face	Dynamic
123	17	121	60	100	0	60	4.40	4.23	1.45	1.27	Flat-face	Dynamic
126	18	124	60	80	0	60	4.40	4.23	1.40	1.30	Flat-face	Dynamic
132	16	130	60	60	0	60	4.40	4.23	1.35	1.27	Flat-face	Dynamic
135	10	133	60	40	0	60	4.40	4.23	1.35	1.30	Flat-face	Dynamic
138	9	136	60	30	0	60	4.40	4.23	1.35	1.30	Flat-face	Dynamic
141	12	139	60	20	0	60	4.40	4.23	1.20	1.35	Flat-face	Dynamic

Run Num	Points	Tare Run	Inclination Angle (Degrees)	Cable Axis Rotation (Degrees)	Turntable Yaw (Degrees)	Phi (Degrees)	Sway (Hz)	Heave (Hz)	Sway (Percent)	Heave (Percent)	Cable Name	Case Type
144	9	142	60	0	0	60	4.40	4.23	1.13	1.22	Flat-face	Dynamic
152	8	150	60	0	0	60	4.40	4.23	2.07	2.01	Flat-face	Dynamic
155	13	153	60	20	0	60	4.40	4.23	2.06	2.09	Flat-face	Dynamic
159	8	157	60	30	0	60	4.40	4.23	2.06	2.09	Flat-face	Dynamic
162	10	160	60	40	0	60	4.40	4.23	2.00	1.97	Flat-face	Dynamic
165	9	163	60	60	0	60	4.40	4.23	1.98	1.95	Flat-face	Dynamic
168	9	166	60	80	0	60	4.40	4.23	1.98	1.88	Flat-face	Dynamic
171	7	169	60	100	0	60	4.40	4.23	2.10	2.00	Flat-face	Dynamic
174	7	172	60	120	0	60	4.40	4.23	1.90	1.88	Flat-face	Dynamic
177	8	175	60	0	90	90	4.40	4.23	1.87	1.85	Flat-face	Dynamic
181	15	179	60	-155	0	60	4.40	4.23	1.97	1.88	IR118E	Dynamic
184	15	182	60	-140	0	60	4.40	4.23	1.98	1.84	IR118E	Dynamic
188	15	185	60	-126	0	60	4.40	4.23	1.97	1.91	IR118E	Dynamic
191	14	189	60	180	0	60	4.40	4.23	1.89	1.88	IR118E	Dynamic
194	14	192	60	-54	0	60	4.40	4.23	1.92	1.87	IR118E	Dynamic
197	15	195	60	0	0	60	4.40	4.23	1.85	1.86	IR118E	Dynamic
201	15	199	60	90	0	60	4.40	4.23	1.87	1.86	IR118E	Dynamic
204	14	202	60	110	0	60	4.40	4.23	1.88	1.84	IR118E	Dynamic
207	15	206	60	130	0	60	4.40	4.23	1.96	1.86	IR118E	Dynamic
211	14	208	60	150	0	60	4.40	4.23	1.87	1.85	IR118E	Dynamic
214	15	212	60	-100	0	60	4.40	4.23	1.89	1.90	IR118E	Dynamic
217	9	215	60	70	0	60	4.40	4.23	1.89	1.85	IR118E	Dynamic
221	10	219	60	134	0	60	4.40	4.23	1.88	1.89	IR118E	Dynamic
224	10	222	60	-105	0	60	4.40	4.23	1.88	1.88	IR118E	Dynamic
227	11	225	60	-105	0	60	4.40	4.23	3.43	3.72	IR118E	Dynamic
230	16	228	60	-126	0	60	4.40	4.23	3.92	3.78	IR118E	Dynamic
233	12	231	60	134	0	60	4.40	4.23	3.90	3.80	IR118E	Dynamic
236	13	234	60	180	0	60	4.40	4.23	3.90	3.70	IR118E	Dynamic
239	26	237	60	180	0	60	4.40	4.23	4.70	4.80	IR118E	Dynamic
242	12	240	60	134	0	60	4.40	4.23	4.80	4.50	IR118E	Dynamic

Run Num	Points	Tare Run	Inclination Angle (Degrees)	Cable Axis Rotation (Degrees)	Turntable Yaw (Degrees)	Phi (Degrees)	Sway (Hz)	Heave (Hz)	Sway (Percent)	Heave (Percent)	Cable Name	Case Type
245	14	243	60	-126	0	60	4.40	4.23	4.50	4.70	IR118E	Dynamic
248	12	246	60	-105	0	60	4.40	4.23	4.80	4.70	IR118E	Dynamic
251	14	249	60	-105	0	60	4.40	4.23	5.90	5.90	IR118E	Dynamic
259	14	257	60	134	0	60	4.40	4.23	5.90	5.90	IR118E	Dynamic
262	11	260	60	-100	0	60	4.40	4.23	3.60	3.70	IR118E	Dynamic
265	24	263	60	-136	32	65	4.40	4.23	3.50	3.60	IR118E	Dynamic
268	16	266	60	-151	47	70	4.40	4.23	3.80	3.70	IR118E	Dynamic
273	12	271	60	-162	59	75	4.40	4.23	3.70	3.60	IR118E	Dynamic
277	22	275	60	-172	70	80	4.40	4.23	3.70	3.60	IR118E	Dynamic
283	20	281	60	170	90	90	4.40	4.23	3.80	3.60	IR118E	Dynamic
287	16	285	60	-172	70	80	4.40	4.23	1.30	1.20	IR118E	Dynamic
290	15	288	60	-136	32	65	4.40	4.23	1.21	1.11	IR118E	Dynamic
296	11	294	60	-136	32	65	4.40	4.23	2.40	2.10	IR118E	Dynamic
299	11	297	60	-106	5	60	4.40	4.23	2.20	2.20	IR118E	Dynamic
302	13	300	60	358	0	60	5.20	4.90	2.40	2.50	LargeCF	Dynamic
306	25	305	60	-80	0	60	4.35	4.17	2.50	2.50	IR113HF	Dynamic
309	16	307	60	-80	0	60	4.35	4.17	1.17	1.22	IR113HF	Dynamic
312	18	310	60	-48	0	60	4.35	4.17	1.22	1.25	IR113HF	Dynamic
315	15	313	60	-28	0	60	4.35	4.17	1.18	1.24	IR113HF	Dynamic
318	16	316	60	10	0	60	4.35	4.17	1.23	1.16	IR113HF	Dynamic
321	17	319	60	35	0	60	4.35	4.17	1.20	1.20	IR113HF	Dynamic
324	18	322	60	45	0	60	4.35	4.17	1.21	1.14	IR113HF	Dynamic
327	16	325	60	50	0	60	4.35	4.17	1.19	1.18	IR113HF	Dynamic
331	16	329	60	55	0	60	4.35	4.17	1.20	1.22	IR113HF	Dynamic
334	17	332	60	100	0	60	4.35	4.17	1.25	1.26	IR113HF	Dynamic
337	21	335	60	63	0	60	4.35	4.17	1.19	1.25	IR113HF	Dynamic
340	14	338	60	63	0	60	4.35	4.17	2.27	2.18	IR113HF	Dynamic
344	14	341	60	100	0	60	4.35	4.17	2.27	2.09	IR113HF	Dynamic
347	14	345	60	50	0	60	4.35	4.17	2.10	2.10	IR113HF	Dynamic
350	14	348	60	49	0	60	4.35	4.17	2.10	2.00	IR113HF	Dynamic

Run Num	Points	Tare Run	Inclination Angle (Degrees)	Cable Axis Rotation (Degrees)	Turntable Yaw (Degrees)	Phi (Degrees)	Sway (Hz)	Heave (Hz)	Sway (Percent)	Heave (Percent)	Cable Name	Case Type
353	10	351	60	49	0	60	4.35	4.17	1.28	1.05	IR113HF	Dynamic
357	14	354	60	49	0	60	4.35	4.17	0.68	0.62	IR113HF	Dynamic
359	14	354	60	50	0	60	4.35	4.17	0.67	0.64	IR113HF	Dynamic
362	16	360	60	63	0	60	4.35	4.17	0.66	0.64	IR113HF	Dynamic
365	15	363	60	100	0	60	4.35	4.17	0.66	0.64	IR113HF	Dynamic
371	14	369	60	-80	0	60	4.35	4.17	0.66	0.64	IR113HF	Dynamic
374	19	372	60	19	32	65	4.35	4.17	0.64	0.65	IR113HF	Dynamic
377	19	375	60	-84	32	65	4.35	4.17	0.64	0.64	IR113HF	Dynamic
380	20	378	60	4	47	70	4.35	4.17	0.66	0.64	IR113HF	Dynamic
383	19	381	60	-7	59	75	4.35	4.17	0.65	0.63	IR113HF	Dynamic
386	19	384	60	-17	70	80	4.35	4.17	0.66	0.63	IR113HF	Dynamic
389	14	384	60	-26	80	85	4.35	4.17	0.65	0.64	IR113HF	Dynamic
392	14	390	60	-35	90	90	4.35	4.17	0.64	0.63	IR113HF	Dynamic
395	14	393	60	-138	90	90	4.35	4.17	0.62	0.63	IR113HF	Dynamic
399	12	396	60	180	0	60	3.77	3.64	4.40	4.40	IR118E	Dynamic
402	13	400	60	180	0	60	4.30	4.17	6.60	6.40	IR118E	Dynamic
410	11	408	60	20	0	60	5.00	4.76	1.60	1.56	Flat-face2	Dynamic
413	17	411	60	80	0	60	5.00	4.76	1.59	1.54	Flat-face2	Dynamic
415	12	414	60	80	0	60	5.00	4.76	1.59	1.54	Flat-face2	Dynamic
418	13	416	60	120	0	60	5.00	4.76	1.62	1.57	Flat-face2	Dynamic
421	9	419	60	20	0	60	5.00	4.76	1.63	1.53	Flat-face2	Dynamic
424	19	422	60	20	0	60	5.00	4.76	1.61	1.56	Flat-face2	Dynamic
427	15	425	60	20	0	60	5.00	4.76	1.61	1.56	Flat-face2	Dynamic
430	23	428	60	20	0	60	5.00	4.76	1.61	1.58	Flat-face2	Dynamic
435	13	433	60	20	0	60	5.00	4.76	1.64	1.52	Flat-face2	Dynamic
440	12	438	60	20	0	60	4.90	4.70	3.28	3.10	Flat-face2	Dynamic
443	17	441	60	20	0	60	4.90	4.70	3.20	3.14	Flat-face2	Dynamic
446	18	445	60	80	0	60	4.90	4.70	3.25	3.00	Flat-face2	Dynamic
449	11	447	60	30	0	60	4.90	4.70	3.26	3.37	Flat-face2	Dynamic
452	16	450	60	10	0	60	4.92	4.72	3.40	3.10	Flat-face2	Dynamic

Run Num	Points	Tare Run	Inclination Angle (Degrees)	Cable Axis Rotation (Degrees)	Turntable Yaw (Degrees)	Phi (Degrees)	Sway (Hz)	Heave (Hz)	Sway (Percent)	Heave (Percent)	Cable Name	Case Type
456	12	454	60	80	0	60	4.92	4.72	3.27	3.14	Flat-face2	Dynamic
459	15	457	60	100	0	60	4.92	4.72	3.32	3.08	Flat-face2	Dynamic
462	10	460	60	120	0	60	4.92	4.72	3.32	3.08	Flat-face2	Dynamic
671	21	668	60	250	90	90	4.92	4.70	0.57	0.41	SIS1	Dynamic
674	19	672	60	240	90	90	4.92	4.70	0.55	0.42	SIS1	Dynamic
677	21	675	60	230	90	90	4.92	4.70	0.56	0.44	SIS1	Dynamic
680	18	678	60	220	90	90	4.92	4.70	0.59	0.42	SIS1	Dynamic
683	17	681	60	210	90	90	4.92	4.70	0.56	0.43	SIS1	Dynamic
686	12	684	60	200	90	90	4.92	4.70	0.59	0.44	SIS1	Dynamic
689	16	687	60	180	90	90	4.92	4.70	0.60	0.42	SIS1	Dynamic
693	19	690	60	80	90	90	4.92	4.70	0.53	0.42	SIS1	Dynamic
696	17	694	60	85	90	90	4.92	4.70	0.54	0.45	SIS1	Dynamic
699	18	697	60	70	90	90	4.92	4.70	0.56	0.44	SIS1	Dynamic
702	19	700	60	30	90	90	4.92	4.70	0.62	0.44	SIS1	Dynamic
708	26	706	60	10	90	90	4.92	4.70	0.64	0.42	SIS1	Dynamic
711	15	709	60	320	90	90	4.92	4.70	0.68	0.43	SIS1	Dynamic
714	9	712	60	210	0	60	4.92	4.70	0.58	0.41	SIS1	Dynamic
720	14	718	60	250	0	60	4.92	4.70	0.76	0.44	SIS1	Dynamic
723	18	721	60	30	0	60	4.92	4.70	0.58	0.40	SIS1	Dynamic
726	17	724	60	214	32	65	4.92	4.70	0.51	0.42	SIS1	Dynamic
729	16	727	60	240	90	90	4.92	4.70	1.22	1.23	SIS1	Dynamic
734	18	735	60	10	90	90	4.92	4.70	1.54	1.24	SIS1	Dynamic
476	18	475	60	20	0	60	0.00	0.00	0.00	0.00	Flat-face	Static
478	21	477	60	10	90	90	0.00	0.00	0.00	0.00	SIS1	Static
480	23	479	60	30	90	90	0.00	0.00	0.00	0.00	SIS1	Static
484	15	483	60	50	90	90	0.00	0.00	0.00	0.00	SIS1	Static
486	22	485	60	50	90	90	0.00	0.00	0.00	0.00	SIS1	Static
488	22	487	60	70	90	90	0.00	0.00	0.00	0.00	SIS1	Static
491	22	490	60	90	90	90	0.00	0.00	0.00	0.00	SIS1	Static
493	22	492	60	170	90	90	0.00	0.00	0.00	0.00	SIS1	Static

Run Num	Points	Tare Run	Inclination Angle (Degrees)	Cable Axis Rotation (Degrees)	Turntable Yaw (Degrees)	Phi (Degrees)	Sway (Hz)	Heave (Hz)	Sway (Percent)	Heave (Percent)	Cable Name	Case Type
495	22	494	60	190	90	90	0.00	0.00	0.00	0.00	SIS1	Static
497	22	496	60	210	90	90	0.00	0.00	0.00	0.00	SIS1	Static
499	22	498	60	230	90	90	0.00	0.00	0.00	0.00	SIS1	Static
501	22	500	60	250	90	90	0.00	0.00	0.00	0.00	SIS1	Static
503	22	502	60	10	0	60	0.00	0.00	0.00	0.00	SIS1	Static
506	22	505	60	30	0	60	0.00	0.00	0.00	0.00	SIS1	Static
508	22	507	60	70	0	60	0.00	0.00	0.00	0.00	SIS1	Static
510	22	509	60	90	0	60	0.00	0.00	0.00	0.00	SIS1	Static
512	22	511	60	250	0	60	0.00	0.00	0.00	0.00	SIS1	Static
514	22	513	60	230	0	60	0.00	0.00	0.00	0.00	SIS1	Static
516	22	515	60	210	0	60	0.00	0.00	0.00	0.00	SIS1	Static
518	22	517	60	190	0	60	0.00	0.00	0.00	0.00	SIS1	Static
519	24	517	60	170	0	60	0.00	0.00	0.00	0.00	SIS1	Static

REFERENCES

1. Bosch, H., and J. Pagenkopf. 2017. "Development of a Robot to Measure Stay Cable Roundness." Presented at the *2017 International Symposium on the Dynamics and Aerodynamics of Cables*. Oct. 30–31. Porto, Portugal.
2. Christiansen H., and G. L. Larose. 2021. *Wind-Tunnel Investigations of the Aerodynamics of Bridge Stay-Cable Cross-sectional Shapes*. Report No. FHWA-HRT-21-074. Washington, DC: Federal Highway Administration.
3. Schewe, G. 1986. "Sensitivity of transition phenomena to small perturbations in flow around a circular cylinder." *Journal of Fluid Mechanics* 172, Nov: 33–46.
4. Christiansen, H. 2016. "Aerodynamics of bridge stay cables—Wind tunnel studies." Ph.D. dissertation UiS no. 294. Department of Mechanical and Structural Engineering and Materials Science, University of Stavanger, Norway.
5. Zdravkovich, M. M. 1997. *Flow Around Circular Cylinders Volume 1: Fundamentals*. Oxford, UK: Oxford University Press.
6. Larose, G. L., and A. D'Auteuil. 2014. *Wind Tunnel Investigations of an Inclined Stay Cable with a Helical Fillet*. Report No. FHWA-HRT-14-070. Washington, DC: Federal Highway Administration.
7. Macdonald, J. H. G., and G. L. Larose. 2006. "A Unified Approach to Aerodynamic Damping and Drag/Lift Instabilities and its Application to Dry Inclined Cable Galloping." *Journal of Fluids and Structures* 22, Feb: 229–252.
8. Kimura, K., T. Kato, and Y. Kubo. 2012. "Aeroelastic Response of an Inclined Circular Cylinder in Smooth and Turbulent Flow." Presented at the *7th International Colloquium on Bluff Body Aerodynamics and Applications*. Shanghai, China.
9. Symes, J., J. Macdonald, and S. Stoyanoff. 2007. "Combined Buffeting and Dry Galloping Analysis of Inclined Stay-Cables." Presented at the *7th International Symposium on Cable Dynamics*, Vienna, Austria.
10. Jones, K. 1992. "Coupled Vertical and Horizontal Galloping." *Journal of Engineering Mechanics* 118, Jan: 92–107.
11. Macdonald, J., and G. L. Larose. 2008. "Two-Degree-of-Freedom Inclined Cable Galloping—Part 1: General Formulation and Solution for Perfectly Tuned System." *Journal of Wind Engineering and Industrial Aerodynamics* 96, March: 291–307.
12. Macdonald, J., and G. L. Larose. 2008. "Two-Degree-of-Freedom Inclined Cable Galloping—Part 2: Analysis and Prevention for Arbitrary Frequency Ratio." *Journal of Wind Engineering and Industrial Aerodynamics* 96, March: 308–326.

13. Den Hartog, J. P. 1932. "Transmission Line Vibration Due to Sleet." *Transactions of the American Institute of Electrical Engineers* 51, Dec: 1074–1076.
14. Stoyanoff, S. 2001. "A Unified Approach for 3D Stability and Time Domain Response Analysis with Application of Quasi-Steady Theory." *Journal of Wind Engineering and Industrial Aerodynamics* 89, Dec: 1591–1606.



Recommended citation: Federal Highway Administration,
Aerodynamic Stability of Bridge Stay Cables—Dynamic Tests and Simulations
(Washington, DC: 2022) <https://doi.org/10.21949/1521926>.

HRDI-40/08-22(WEB)E